Assessment of Atmospheric and Oceanographic Measurements from an Autonomous Surface Vehicle

ANDRE AMADOR,[a] SOPHIA T. MERRIFIELD,[a] AND ERIC J. TERRILL[a]

[a] *Scripps Institution of Oceanography, La Jolla, California*

ABSTRACT: The present work details the measurement capabilities of Wave Glider autonomous surface vehicles (ASVs) for research-grade meteorology, wave, and current data. Methodologies for motion compensation are described and tested, including a correction technique to account for Doppler shifting of the wave signal. Wave Glider measurements are evaluated against observations obtained from World Meteorological Organization (WMO)-compliant moored buoy assets located off the coast of Southern California. The validation spans a range of field conditions and includes multiple deployments to assess the quality of vehicle-based observations. Results indicate that Wave Gliders can accurately measure wave spectral information, bulk wave parameters, water velocities, bulk winds, and other atmospheric variables with the application of appropriate motion compensation techniques. Measurement errors were found to be comparable to those from reference moored buoys and within WMO operational requirements. The findings of this study represent a step toward enabling the use of ASV-based data for the calibration and validation of remote observations and assimilation into forecast models.

KEYWORDS: Acoustic measurements/effects; In situ atmospheric observations; In situ oceanic observations; Instrumentation/sensors; Surface observations; Automated systems

1. Introduction

a. Advancing oceanographic measurements from autonomous surface vehicles

Understanding the state of the ocean and its associated impact on weather and climate drives the need for comprehensive and sustained ocean observations. In particular, the exchange of heat, mass, momentum, and energy across the air–sea boundary plays a crucial role in Earth's weather and climate (Yu 2019; Cronin et al. 2019). Central to these exchanges are a myriad of small-scale physical processes that are typically represented in large-scale weather, ocean, and climate forecast models by measurement-based parameterizations (Edson et al. 2007; Cronin et al. 2019). Accurate meteorological and oceanographic measurements are thus fundamental for the quantification of key ocean properties at the air–sea interface and the reliable representation of the associated fluxes in model simulations. To fulfill this need, the scientific community relies on measurements from satellite-based and in situ ocean sensors. Yet, the broad range of spatial and temporal scales associated with ocean–atmospheric dynamics poses operational challenges for both technologies. As a result, many regions of the ocean surface remain critically undersampled (Lindstrom et al. 2012; Centurioni et al. 2019).

Over the past decade, a new class of environmentally propelled autonomous surface vehicles (ASVs) has emerged as a key enabling technology for the ocean observing mission. Prominent examples of commercially available ASVs include the Saildrone (Gentemann et al. 2020), the Sailbuoy (Ghani et al. 2014; Hole et al. 2016), the AutoNaut (Johnston and Poole 2017), and the Wave Glider (Hine and McGillivary 2007). A key feature of these marine robotic systems is their ability to withstand harsh conditions at sea over long periods of time (Delory and Pearlman 2018). ASVs enable long duration deployments by harnessing abundant wind or wave energy for propulsion, and are capable of navigating autonomously between prescribed waypoints without the need for real-time human input or control. ASVs can target flow features (e.g., fronts, eddies) either autonomously via adaptive sampling algorithms (e.g., Zhang et al. 2019) or under the supervision of remote human pilots (e.g., Thomson and Girton 2017). Another important characteristic of ASVs is their ability to operate around a fixed station while gathering Eulerian-like time series data, similar to a moored asset.

Wave Gliders, in particular, are optimally designed to observe air–sea interactions. Although slow moving (speeds of 0.5–1.5 m s^{-1} are typical), Wave Glider ASVs offer a number of unique advantages over traditional in situ ocean observing platforms (e.g., ships, moored buoys, and Lagrangian drifters). They are far less expensive to operate than research vessels and generally less intrusive than ships when making measurements (e.g., Wave Gliders have minimal flow distortion) (Grare et al. 2021). In contrast to moored buoys, Wave Gliders can collect measurements over broad spatiotemporal scales, elucidating interesting spatial gradients fixed assets cannot resolve. Surface drifters offer both spatial and temporal coverage, but their inherently Lagrangian nature limits them; drifters tend to collect in convergent zones (e.g., fronts) or can remain trapped in eddies for extended periods of time, leading them to oversample these regions (D'Asaro et al. 2018; Pearson et al. 2019, 2020). Wave Gliders can thus help fill a critical gap in ocean science observations, particularly

Corresponding author: Andre Amador, a1amador@ucsd.edu

in remote areas where persistent measurements are scarce and difficult to obtain with traditional sampling techniques (Merrifield et al. 2019). ASV technologies are still in the pilot phase (e.g., see Lindstrom et al. 2012); thus, our detailed examination of the Wave Glider data quality is applicable to this entire class of vehicles.

Several studies have explored the utility of environmental measurements collected aboard Wave Glider ASVs (Mullison et al. 2011; Lenain and Melville 2014). More recently, Thomson et al. (2018) and Grare et al. (2021) present measurements from Wave Glider ASVs over a range of field conditions. Specifically, the work of Thomson et al. (2018) examines measurements of wind stress, bulk winds, and directional wave spectra from a Wave Glider. Expanding on this work, Grare et al. (2021) compares Wave Glider measurements of water temperature, surface waves, water velocity profiles, and several atmospheric variables with concurrent observations from both the R/P *FLIP* and the R/V *Sally Ride*. Overall, strong agreement is reported with the reference data, albeit with some discrepancies in wind and current measurements that are justified in terms of spatial variability and misalignment of the wind sensor with the compass. These papers identified further research is required to determine the extent to which wave shadowing affects the vehicle's bulk wind measurements. In addition, the role of the wave encounter angle on Wave Glider measurements of the wave spectrum and mean wave direction is not fully understood. Although the potential impacts of Doppler shifting were noted by Thomson et al. (2018), corrections for surface wave Doppler effects have yet to be formalized and implemented for Wave Glider observations. Furthermore, a detailed assessment of the Wave Glider ADCP measurement accuracy and bias due to platform motion is missing.

This study addresses these platform-motion shortcomings and further evaluates the capabilities of Wave Glider ASVs for sensing the environment. Our evaluation draws on data collected in a series of field deployments conducted off the coast of Southern California from May 2020 to December 2021 (Fig. 1). The primary objective of these missions was to assess the use of ASV-based sensing technologies to support data collection efforts for a long-standing fisheries and oceanography program based in Southern California (California Cooperative Oceanic Fisheries Investigations; Bograd et al. 2003). Real-time adaptive sampling and onboard routing capabilities were used in our deployments (e.g., Amador et al. 2021; Young et al. 2021). Our approach involved operations in close proximity to fixed National Data Buoy Center (NDBC), Coastal Data Information Program (CDIP), and Scripps Institution of Oceanography (SIO) moored buoy assets, which provided standard measurements.

b. Wave Glider

The Boeing Liquid Robotics SV3 Wave Glider (Figs. 1d, 2) is a wave-propelled ASV composed of a 2.20-m-long submersible glider (sub) and a 3.05-m surface float. Forward thrust is generated by transferring the float's wave-induced vertical (heave) motions to the sub through an 8-m umbilical tether that connects the two components together. Hinged and spring-loaded hydrofoil fins mounted on the sub mechanically convert the wave-induced vertical displacements into a hydrodynamic force that propels the vehicle forward. Steering is achieved through a directional rudder mounted on the sub. The sub also features an electric thruster for supplementary propulsion. A command and control interface, known as the Wave Glider Management System (WGMS), enables the operator to remotely send navigational waypoints and course commands to the vehicle in real time via cell or Iridium satellite link.

The Wave Glider is designed to support a wide variety of meteorological and oceanographic sensors and payloads that can be mounted on the float or the sub. The SV3 float has three main payload bays that house the Sensor Management Computer (SMC), the navigation computer, auxiliary power units, and supporting electronics. A photovoltaic system with three 64-W solar panels mounted on the float supplies power to payload electronics, sensors, and the auxiliary thruster. The Wave Gliders operated by the Coastal Observing Research and Development Center (CORDC) are outfitted with a Seabird conductivity–temperature–depth (CTD) sensor, a downward-looking acoustic Doppler current profiler (ADCP), and the CORDC-fabricated meteorological and waves sensing payloads. We note that Liquid Robotics offers comparable sensor packages (i.e., GPSwaves, Airmar weather station, and ADCP processing) for off-the-shelf vehicles as a commercial option. Here, however, we implement and validate our own sensing solutions to ensure consistent and reliable performance. A more detailed account of the onboard instrumentation and associated measurement techniques is given in the following sections.

2. Meteorological measurements

a. Instrumentation and raw data

Wave Glider meteorological measurements were collected using the CORDC-fabricated environmental sensing suite, a variant of the Expeditionary Meteorological (XMET) system (Rogowski et al. 2021). Similar to the XMET, the package is an entirely self-contained unit capable of global bidirectional communications. It features a Vaisala WXT520 weather sensor mounted on a vertical mast on the float (Fig. 2). A waterproof weather station located on the central payload bay of the vehicle houses the data acquisition and telemetry systems and supporting electronics.

Measurements of atmospheric pressure, air temperature, and bulk winds are made at 1.2 m above the sea surface. The wind sensor uses three equally spaced ultrasonic transducers to derive horizontal wind speed and direction. A Revolution GS electronic compass (True North Technologies) is used to project the observed wind velocity vector onto a local east–north–up (ENU) Cartesian coordinate system. Pressure and temperature are measured via capacitive silicon and ceramic sensors, respectively (Vaisala 2012).

The sensors were configured to sample at 1 Hz and average observations in 10-min blocks. Following the 10-min collection period, a 4-min window was used for onboard processing and
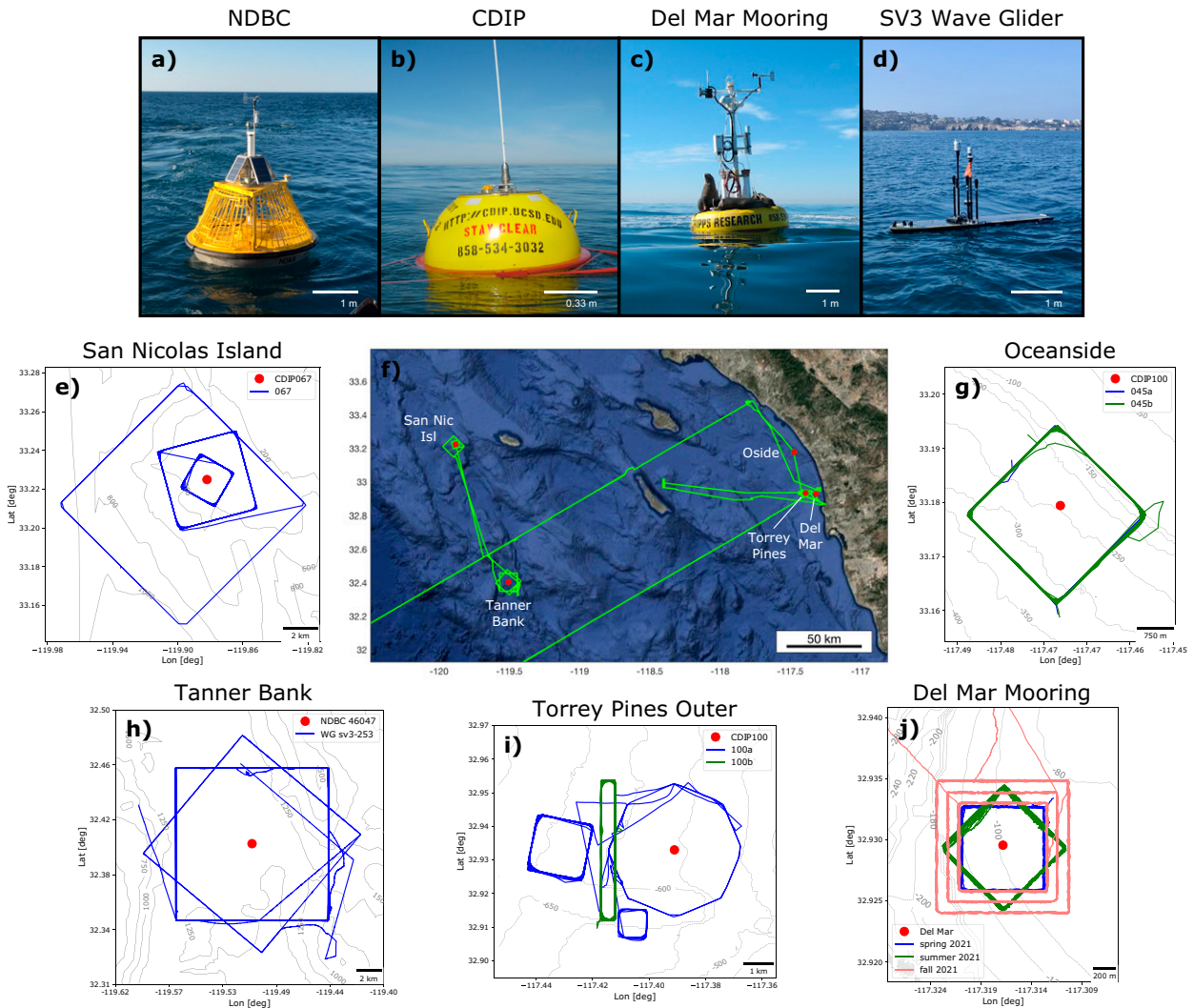
FIG. 1. (a)–(d) Observational assets, (f) satellite image (Google Earth) of study area, and (e),(g)–(j) survey regions overlaid with bathymetry. Location of control assets (bold red circles) and tracks followed by the Wave Gliders during comparison surveys (colored lines) are indicated.

near-real-time telemetry. Raw meteorological data were stored in a compact flash (CF) card, and near-real-time burst-averaged observations were transmitted back to shore via Iridium short burst data (SBD). Translational motion correction and additional postprocessing routines were carried out shoreside as described in the following section.

b. Motion compensation and 10-m wind speed adjustment

Edson et al. (1998) identify three sources that can lead to motion contamination of the wind signal: 1) instantaneous heading and tilt angles (i.e., pitch and roll) of the wind sensor, 2) angular velocities at the sensor location, and 3) translational velocities. Here, our goal is to determine the true (i.e., not contaminated by platform motion) mean wind estimates. We assume a properly ballasted float with pitch and roll variations that are symmetrically distributed around a near-zero

mean over the averaging interval (statistical analysis of the float's pitch and roll motions establish that these assumptions are valid in our case). Sensor tilts and the associated angular velocities are thus expected to provide a negligible contribution to the burst-averaged true wind estimates. For burst-averaged measurements, the mean vertical velocity of the platform is zero and therefore neglected.

Considering the above assumptions, the Wave Glider's burst-averaged wind measurements are motion corrected as follows:

$$
\begin{aligned}
u_{\text{true}} &= u_{\text{app}}\cos\psi + v_{\text{app}}\sin\psi + u_{\text{mot}}, \\
v_{\text{true}} &= -u_{\text{app}}\sin\psi + v_{\text{app}}\cos\psi + v_{\text{mot}},
\end{aligned}
\tag{1}
$$

where u_{true} and v_{true} are the zonal (west–east) and meridional (south–north) velocity components relative to a fixed (i.e., Earth) reference frame, u_{app} and v_{app} are the apparent wind velocities in the platform reference frame, and ψ is the platform heading
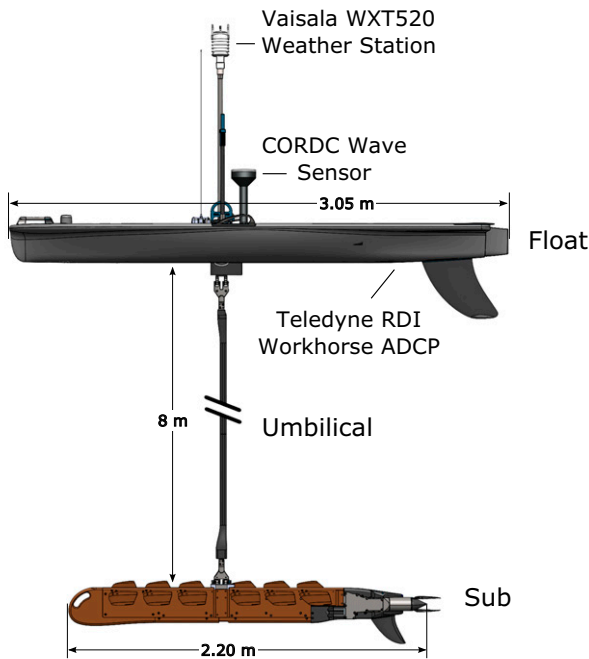
FIG. 2. SV3 Wave Glider diagram showing its main components, associated dimensions, and relevant instrumentation.

(positive for the float's bow yawed clockwise from north). The Wave Glider's translational velocities (u_{mot} and v_{mot}) are computed from GPS endpoint coordinates over the averaging interval. The meteorological wind direction is computed by taking the four-quadrant arctangent of the negative east and negative north velocity components of the true wind.

The resulting true wind estimates are adjusted to a reference height of 10 m assuming a logarithmic wind profile

$$u_z = \frac{u_*}{\kappa} \ln\left(\frac{z}{z_0}\right), \tag{2}$$

where u_z is the wind speed at a height z, u_* is the friction velocity, $\kappa = 0.4$ is the von Kármán constant, and z_0 is the roughness scale. The friction velocity is given by

$$u_* = \sqrt{C_{DN}}\, u_{10}, \tag{3}$$

where C_{DN} is a nondimensional drag coefficient for neutrally stratified conditions at 10 m and u_{10} is the associated 10-m wind speed. With the observed wind speed and measurement height (e.g., $z = 1.2$ m for Wave Glider), we eliminate z_0 via

$$u_z - u_{10} = \frac{u_*}{\kappa} \ln\left(\frac{z}{10}\right), \tag{4}$$

and obtain u_{10} by solving (4) and (3) iteratively using C_{DN} values given by Large and Pond (1981). It should be noted that more complex and advanced parameterization schemes have been proposed (e.g., Fairall et al. 2003; Edson et al. 2013), but these are not applied here for the sake of simplicity.

c. Meteorological dataset

Meteorological data were collected between 20 June and 10 July 2020 near the Tanner Bank buoy (NDBC 46047) to characterize the quality of the Wave Glider measurements. The Tanner Bank buoy is located in the Southern California Bight, approximately 224 km west of San Diego (32.388°N, 119.525°W) and features a Self-Contained Ocean Observations Payload (SCOOP) (Kohler et al. 2015) installed on a 3-m discus hull (Fig. 1a). The SCOOP system at Tanner Bank is instrumented with a Gill MetPak meteorological sensor that measures air temperature, pressure, humidity, wind speed and direction. Air pressure and temperature are measured at 2.4 and 3.4 m above mean sea level, respectively. Wind speed and direction are measured using a four-blade, impeller-driven, wind-vane sensor located 3.8 m above mean sea level. While primarily meteorological, the Tanner Bank buoy is also outfitted with a wave-sensing payload and thermistor for measuring sea surface temperature. The Tanner Bank station transmits averaged meteorological observations to NDBC every 10 min, and reports wave spectra and bulk wave statistics hourly. NDBC employs automated quality control procedures and routinely recalibrates buoy sensors to ensure the accuracy of the measurements (Corredor 2018).

As depicted in Fig. 1h, the Wave Glider was programmed to repeat a 12 km × 12 km square box centered around the buoy for roughly 19 days. Vehicle speeds (averaged over 10 min) ranged from about 0.1 to 1.5 m s^{-1}, with a mean speed of 0.51 m s^{-1}. The observations at Tanner Bank spanned a range of sea states and meteorological conditions, with significant wave heights and wind speeds ranging between 1 and 3.5 m and 1 and 12 m s^{-1}, respectively. The prevailing wind direction was generally from the west-northwest over the duration of the experiment. Field data from both platforms are presented and compared in section 2d.

To enable comparisons, meteorological data were processed as follows. Barometric pressure measurements from both platforms were adjusted to sea level following the procedures described in WBAN (U.S. Weather Bureau 1963). Vehicle-based, burst-averaged wind measurements were motion compensated and adjusted to a 10-m reference height assuming a logarithmic wind profile (section 2b). Buoy wind measurements were also brought up to a height of 10-m in similar fashion. Variable wind data, defined here as having a standard deviation greater than 30° over a 10-min interval, were discarded to eliminate instances with poorly defined mean wind direction. Wind data records with turning maneuvers were also excluded from the analysis. These screening criteria limit the amount of valid wind data to about 96% of the total bursts. All meteorological measurements were temporally averaged into 30-min intervals and interpolated onto a common time base.

d. Evaluation of meteorological measurements

In this section, we compare observations from the Wave Glider to meteorological measurements collected by the Tanner Bank buoy (NDBC 46047) over a 19.2-day period to assess the vehicle's capabilities for research-standard accuracy. As indicated in section 2c, buoy measurements serve as
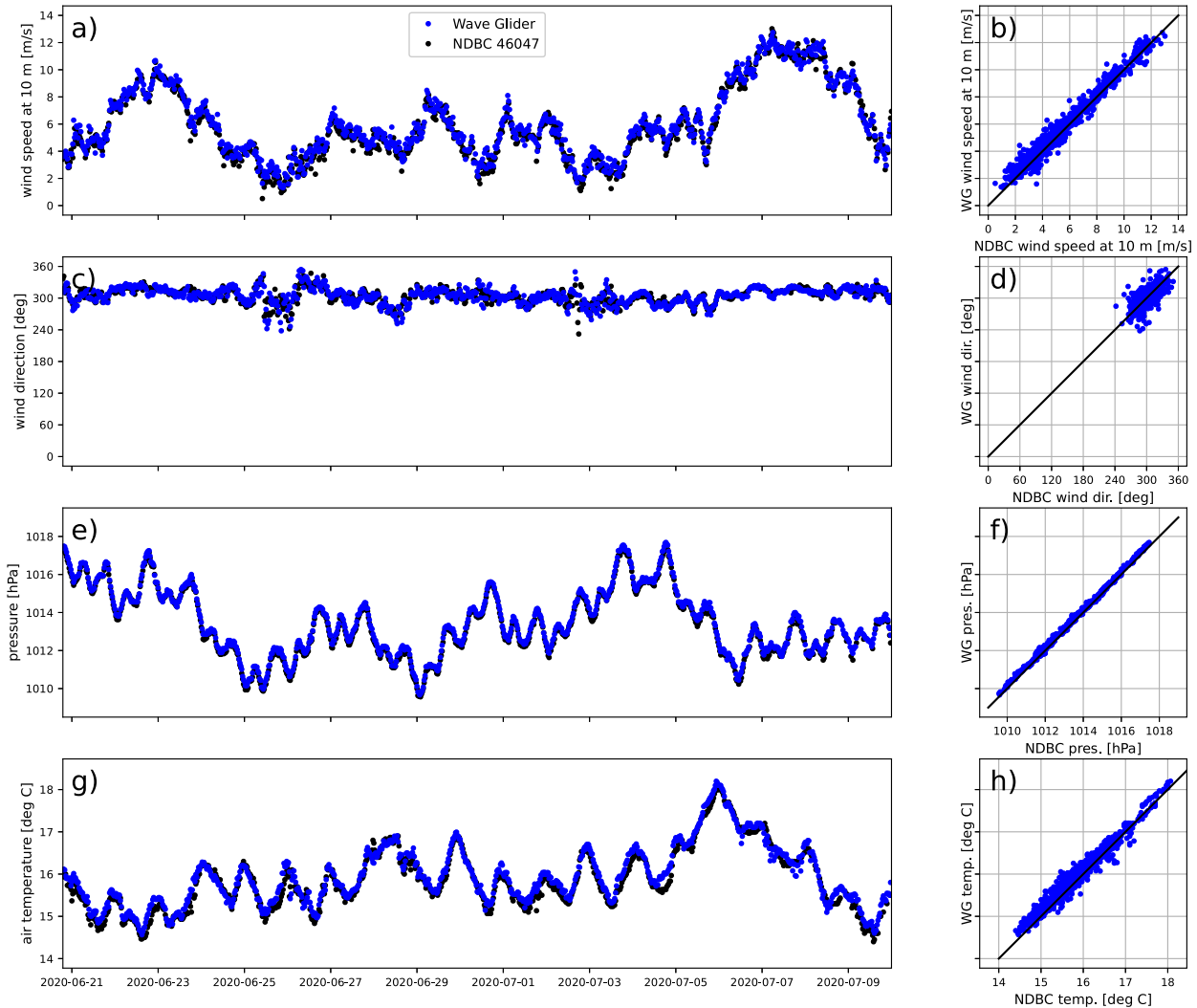
FIG. 3. Time series and scatterplot comparisons of (a),(b) 10-m wind speeds, (c),(d) wind direction, (e),(f) sea level pressure, and (g),(h) air temperature from Wave Glider- (blue) and NDBC-based (black) observations at Tanner Bank. Black lines in (b), (d), (f), and (h) correspond to a one-to-one relationship.

control data in the evaluation experiment. Time series and scatterplot comparisons of the observed meteorological quantities are presented in Fig. 3; the resulting error statistics are provided in Table 1.

The meteorological measurements obtained by the Wave Glider are in excellent agreement with those reported by the NDBC buoy at Tanner Bank (Fig. 3). For the wind measurements (Figs. 3a–d), speed and direction errors were reduced

by 45% and 16%, respectively, via motion compensation procedures. Although there are episodic differences in the measured wind field, no appreciable biases were detected between the Wave Glider and the buoy in terms of wind speed and direction (Table 1). Close examination of Figs. 3a and 3c reveals that periods of low wind speed result in higher variability for the observed wind directions, which in turn lead to more pronounced deviations between the Wave Glider and the buoy.

TABLE 1. System accuracies and WMO (2008) standards for observed atmospheric variables during the Tanner Bank 19-day evaluation period.

Measurement	RMSE	Bias	NDBC reported accuracy	WMO requirement
Wind speed (m s^{-1})	0.52	0.22	0.55	0.5
Wind direction (°)	10.6	2.90	9.3	10
Sea level pressure (hPa)	0.17	0.11	0.07	0.2
Air temperature (°C)	0.19	0.09	0.09	0.2

These discrepancies at lighter wind speeds suggest the dominance of local processes over the synoptic-scale pressure gradient in determining the wind direction. It is also worth noting that wave sheltering effects were not evident in the Wave Glider winds despite the comparable elevation of the onboard anemometer (1.2 m) and the observed significant waves (1–3.5 m, not shown). As seen in Figs. 3a and 3b, the accuracy of the Wave Glider wind speed measurement does not depend on the magnitude of the observed wind field, which was well correlated with the wave heights in this case. We further discuss the lack of wave sheltering effects in section 5a.

As shown in Fig. 3e, small diurnal and semidiurnal pressure oscillations resulting from the atmospheric thermal tide are well captured by the vehicle's meteorological package. Diurnal air temperature variations driven by solar radiative heating are also evident in the measurements (Fig. 3g). The Wave Glider measurements of sea level pressure and air temperature exhibit small biases of 0.11 hPa and 0.09°C, respectively (Table 1). Further analysis reveals that differences between the Wave Glider and the control sensor temperatures do not vary significantly between nighttime and daytime hours, indicating that the WXT520 weather station can adequately shield against solar radiation. There was no evidence that the accuracy of the pressure and temperature readings was compromised by exposure to sea spray and ensuing salt accretion.

A quantitative assessment of the comparisons is provided in Table 1 along with the reported NDBC uncertainties (NDBC 2009) and the maximum acceptable operational uncertainties in accordance with WMO (2018) regulations for the considered atmospheric variables. We compute the relative error of the Wave Glider and buoy measurement system via the standard definition of root-mean-square error (RMSE), which accounts for the instrumental and environmental variability as well as systematic biases. The mean bias error is also presented in Table 1 as a separate quantity to indicate the overall direction of the error. The bias is computed as the Wave Glider observations minus the NDBC reference data.

Our results confirm that Wave Glider relative errors are comparable to the typical measurement uncertainties of operational NDBC buoys (Table 1). Considering the reported NDBC uncertainties and the effects of spatial variability, we expect that the vehicle's actual measurement errors (i.e., those relative to the true ambient values) should be lower than those presented in Table 1. Furthermore, systematic errors were found to be similar to standard errors (computed by dividing the RMSE by the square root of the effective number of degrees of freedom in the dataset), suggesting that the observed biases may be negligible. In light of the above analysis, we conclude that the Wave Glider meteorological measurements can reliably achieve the operational accuracy standards required by the WMO (2018).

3. Wave measurements

a. Instrumentation and raw data

The Wave Gliders used in this study were equipped with the CORDC-fabricated directional wave sensor (Fig. 2), a compact, low-cost unit equipped with a u-blox M8 GNSS receiver, an Iridium modem, a microSD card, and a low-power microcontroller. The system uses Doppler shift derived GPS velocity signals ($\sim$5 cm s^{-1} accuracy) to determine the float's motions. The sensor package was adapted to fit (1 modular payload unit form factor with dimensions 12 cm $\times$ 41 cm $\times$ 54 cm) and draw power from the Wave Glider. It also incorporates a raised antenna to limit overwash.

The Wave Glider wave sensors were configured to sample three-axis Doppler velocity time series (hereafter referred to as u, v, and w for east, north, and vertical velocity components, respectively) continuously at 2 Hz. Raw data samples were collected using $N = 1024$ (512 s) bursts and processed on board. The resulting spectra and bulk wave statistics were transmitted in near–real time via Iridium SBD. Velocity time series were also retrieved from the internal data storage card upon recovery.

b. Spectral analysis

To compute wave spectra, GPS velocities (u, v, w) are first detrended in the time domain and partitioned into three $n = 512$-point (256 s) overlapping segments (50% overlap). Each segment is multiplied by a Hanning window (time-domain weighting) and rescaled appropriately to conserve its original variance. A fast Fourier transform (FFT) is then applied to these data to produce complex Fourier coefficients at each frequency (f); the negative half of the frequency spectra are discarded. Auto- and cross-spectra are subsequently computed for all possible FFT output pairs as follows:

$$S_{ii}(f) = 2S_i(f)S_i^*(f),$$
$$S_{ij}(f) = 2S_i(f)S_j^*(f), \qquad (5)$$

where $S_i^*(f)$ is the complex conjugate of $S_i(f)$ and the subscripts i and j ($i \neq j$) are indices for u, v, or w velocities. The factor of 2 in (5) preserves the variance of the two-sided spectral density functions when using one-sided spectra. Spectra resulting from the $n = 512$-point (256 s) overlapping segments are ensemble averaged to produce smoothed auto- and cross-spectral estimates for each burst. All spectral quantities are band averaged into 68 frequency bands, ranging in resolution as follows: 0.0039 Hz for $0.0039 \leq f \leq 0.1367$, 0.0156 Hz for $0.1406 \leq f \leq 0.6094$, and 0.0312 Hz for $0.6250 \leq f \leq 0.9062$ Hz. These spectra are later trimmed to exclude frequencies outside of the dominant sea-swell frequency band $0.05 < f < 0.50$ Hz (or equivalently, wave periods $2 < T < 20$ s).

The sea surface elevation spectrum $E(f)$ is estimated from the vertical velocity autospectrum using linear wave theory:

$$E(f) = \frac{S_{ww}}{(2\pi f)^2}. \qquad (6)$$

In the deep water limit (a reasonable approximation for the data considered here), linear waves have circular orbits such that $S_{ww} = S_{uu} + S_{vv} = (2\pi f)^2 E$. However, this theoretical equality may not hold for Wave Glider observations since wave propulsion contributes nonorbital motions to the horizontal velocity measurements (Thomson et al. 2018). Hence,

in this case, the calculation of $E(f)$ from S_{ww} [Eq. (6)] is favored over $E = (S_{uu} + S_{vv})/(2\pi f)^2$ because it avoids propulsive biases that overlap in frequency space with surface gravity waves. Note that converting velocity spectra into elevation spectra via (6) amplifies noise at low frequencies, which complicates the measurement of small amplitude low-frequency waves that disappear below sensor noise.

c. Directional analysis

Estimates of mean wave direction and directional spread are computed from normalized velocity quad spectra (imaginary part of the cross-spectra) following the work of Kuik et al. (1988) (see also Long 1980; Herbers et al. 2012) with minor modifications. The lowest-order moments of the directional energy distribution are given by

$$a_1(f) = \frac{\text{Im}[S_{wu}]}{\sqrt{S_{ww}(S_{uu} + S_{vv})}}, \tag{7}$$

$$b_1(f) = \frac{\text{Im}[S_{wv}]}{\sqrt{S_{ww}(S_{uu} + S_{vv})}}, \tag{8}$$

and the mean wave direction (θ) and spread (σ_θ) are determined by

$$\theta(f) = 270 - \frac{180}{\pi}\arctan 2(b_1, a_1), \tag{9}$$

$$\sigma_\theta(f) = \frac{180}{\pi}\sqrt{2\left(1 - \sqrt{a_1^2 + b_1^2}\right)}, \tag{10}$$

where θ is measured in degrees clockwise from north and represents the direction the waves are coming from. For angles smaller than 0° or larger than 360° we add or subtract 360°, respectively, to ensure that $0° \leq \theta \leq 360°$. The directional spread (σ_θ) can be interpreted as the standard deviation of wave angles.

d. Doppler correction of wave spectra

The relative motion between the incident wave field and the moving platform introduces a Doppler shift to the observed wave frequencies (e.g., Drennan et al. 1994; Hanson et al. 1997; Cifuentes-Lorenzen et al. 2013; Collins et al. 2017). Here, the derivation of Doppler corrections for wave frequency spectra follows closely the work of Collins et al. (2017), but allows for variations in θ as a function of frequency. We assume a constant vehicle speed and direction. The validity of these assumptions is examined in section 3g(1) and further discussed in section 5b.

For a surface platform moving at constant speed (u_{ob}) and direction, the observed wave frequencies (f_{ob}) will be Doppler shifted according to

$$f_{\text{ob}} = f_{\text{in}} + \frac{ku_{\text{ob}}}{2\pi}\cos(\theta_r), \tag{11}$$

where f_{in} is the intrinsic wave frequency, k is the wavenumber (invariant between reference frames) (Drennan et al. 1994),

and θ_r is the relative encounter angle between the mean wave direction and the vehicle's course over ground (COG) at each frequency. We take $\theta_r = 0°$ and $\theta_r = 180°$ for head and following seas, respectively. Hence, observed frequencies will be shifted higher (and lower) for head (and following) seas as the vehicle experiences an increase (or decrease) in wave encounter events relative to a stationary observer; that is, $f_{\text{ob}} > f_{\text{in}}$ for head seas and $f_{\text{ob}} < f_{\text{in}}$ for following seas.

Considering deep water waves, the dispersion relation as given by linear wave theory, can be expressed as

$$k = \frac{(2\pi f_{\text{in}})^2}{g}, \tag{12}$$

where $g = 9.8$ m s^{-2} is the acceleration due to gravity. By substituting (12) into (11) and solving the resulting quadratic equation, we can obtain a relationship for f_{in} in terms of the apparent frequency:

$$f_{\text{in}} = \frac{-g \pm \sqrt{g^2 + 8\pi g u_{\text{ob}}\cos\theta_r f_{\text{ob}}}}{4\pi u_{\text{ob}}\cos\theta_r}. \tag{13}$$

As pointed out by Collins et al. (2017), the intrinsic wave spectra (S_{in}) can be expressed in terms of the observed spectra (S_{ob}), but the spectral energy (or total variance) must be conserved in the transformation. This can be mathematically expressed as

$$S_{\text{in}}(f_{\text{in}}) = S_{\text{ob}}(f_{\text{ob}})\frac{\delta f_{\text{ob}}}{\delta f_{\text{in}}}, \tag{14}$$

where $\delta f_{\text{ob}}/\delta f_{\text{in}}$ is the Jacobian and δ represents the frequency bandwidth determined here by finite central differencing. We apply this Doppler correction to the velocity autospectra (S_{uu}, S_{vv}, S_{ww}) and quad spectra of horizontal and vertical velocities ($\text{Im}[S_{wu}]$, $\text{Im}[S_{wv}]$) at each frequency band and subsequently recompute all spectrally derived parameters (E, a_1, b_1, θ, and σ_θ).

e. Computation of bulk wave parameters

Bulk wave parameters were estimated from Doppler-corrected sea surface elevation spectra over the dominant sea-swell frequency band (2–20 s) using conventional definitions (e.g., Holthuijsen 2010). The significant wave height (H_s) is computed by

$$H_s = 4\sqrt{\int_{f_a}^{f_b} E(f)df}, \tag{15}$$

where $f_a = 0.05$ Hz and $f_b = 0.5$ Hz are the lower- and upper-frequency limits, respectively. The peak period (T_p) is the inverse of the frequency at the highest energy density in $E(f)$ and the peak wave direction (θ_p) is the value of the mean wave direction at the peak period. In addition to T_p and θ_p, we compute energy-weighted estimates for wave period

$$T_e = \frac{\int_{f_a}^{f_b} E(f)df}{\int_{f_a}^{f_b} fE(f)df}, \tag{16}$$

and wave direction

TABLE 2. Overview of wave evaluation datasets. Dataset ID labels are based on the CDIP station identifier.

Dataset ID	CDIP station	Wave Glider	Dates	Duration (days)
100a	Torrey Pines Outer	SV3-253	9–15 May 2020	5.8
045a	Oceanside Offshore	SV3-253	24–25 May 2020	1.4
067	San Nicolas Island	SV3-253	12–18 Jun 2020	6.2
100b	Torrey Pines Outer	Magnus	2–9 Jul 2020	7.8
045b	Oceanside Offshore	Magnus	10–16 Jul 2020	5.3

$$\theta_e = \tan^{-1}\left\{\frac{\int_{f_a}^{f_b} E(f)\sin[\theta(f)]df}{\int_{f_a}^{f_b} E(f)\cos[\theta(f)]df}\right\}, \qquad (17)$$

to allow for more robust comparisons in mixed seas, which tend to result in multipeaked spectra. Energy-weighted metrics are arguably better suited for comparisons than peak values because they are unaffected by the peak-picking issues that can arise, for instance, in bimodal sea states with approximately equal sea and swell energy.

While not employed in this study, it is worth noting that several spectral partitioning techniques have been developed for the identification of wind sea and swell (e.g., see Portilla et al. 2009, and references therein). The most robust algorithms make use of the full 2D spectra as well as the local wind speed and direction. Wave Gliders are thus particularly well-suited for this task, as they are commonly instrumented with both wind and directional wave sensors. The eventual adaptation of such methods to Wave Glider observations and their use in near–real time would improve the characterization of sea states (relative to the conventional description by bulk wave statistics) and provide more insight into the evolution of wave systems originating from different sources.

f. Wave evaluation datasets

Observations from various Datawell Directional Waverider (DWR) buoys operated by CDIP were used to evaluate the Wave Glider measurements. DWRs are spherical (0.9-m diameter) surface following buoys equipped with a motion sensor package that collects acceleration, pitch, roll, and heading data to produce estimates of directional wave spectra and bulk wave parameters. Vertical accelerometers mounted on a gravity-stabilized platform enable the straightforward estimation of heave displacements. Raw data are collected at 1.28 Hz for 20 min, processed on board, transmitted to shore-based servers via Iridium, and reported by CDIP in near–real time every 30 min. DWRs have been extensively tested over the last three decades in numerous wave intercomparison studies (e.g., O'Reilly et al. 1996; Hauser et al. 2005; Collins 2012), and remain the instrument of choice for directional wave measurements.

Wave evaluation surveys typically lasted between 1 and 7 days with the Wave Gliders collecting data at reasonable proximity to the buoys (<10 km). We examine here five datasets gathered in the Southern California region (Figs. 1e,i,g and Table 2). The datasets span a wide variety of sea states,

including both swells and locally generated wind waves (see section 3g). The San Nicolas Island buoy dataset (067) is given particular attention in section 3g(1) as it was designed to be aligned with the dominant wave direction; thus, it is used to emphasize the presence of a Doppler shift in the Wave Glider observations of the surface wave field. The evaluation of Wave Glider estimates of mean wave direction [section 3g(2)] draws on the 100a and 067 datasets to characterize the quality of the wave directional measurements in both swell- and wind-dominated sea states. Finally, all datasets are considered in the bulk wave parameter evaluation conducted section 3g(3).

g. Evaluation of wave measurements

1) WAVE SPECTRA

We focus below on an example drawn from the San Nicolas Island buoy (CDIP 067 and NDBC 46219) dataset (067 in Table 2) to evaluate the effects of vehicle motion on Wave Glider spectra. We also examine the validity of using constant vehicle speed and direction as a practical assumption to correct for Doppler effects (see section 3d). Wave Glider spectra, computed from (6), were interpolated onto CDIP frequencies and time averaged to match CDIP's 30-min reporting interval. Data records containing turning maneuvers were discarded.

Wave energy density spectrograms, derived from Wave Glider- and CDIP-based observations, highlight the effects of vehicle motion and wave encounter angle on the vehicle measurements (Figs. 4a,b,d). As described in section 3f, the Wave Glider was programmed to navigate around the buoy in a series boxes aligned with the wave direction over the observational period (Fig. 1e). A comparison of the spectrograms in Figs. 4b and 4d reveals frequency modulations in Wave Glider spectra (Fig. 4b) that are absent from the control dataset (Fig. 4d). As evidenced by the variations in vehicle heading and wave encounter angle (Fig. 4a), the observed frequency shifts vary in synchrony with the vehicle's trajectory around the buoy and the resulting platform motion relative to the wave field. Initially, the observed shifts vary at shorter time intervals (12–15 June 2020), coincident with the smallest boxes depicted in Fig. 1e. Note that the frequency modulations appear to dilate for the second half of the record (15–18 June 2020), as the box-shaped course enlarged (Fig. 1e). Furthermore, energy shifts toward higher and lower frequencies can be observed in Fig. 4b for head ($\theta_r = 0°$) and following ($\theta_r = \pm180°$) seas (Fig. 4a), respectively, indicating directional agreement with the expected effects of Doppler shifting.

To examine these phenomena more closely, energy-weighted wave period estimates from the Wave Glider (T_{eWG}) and the San Nicolas Island CDIP buoy (T_{eCDIP}) are calculated, and their differences ($\Delta T_e = T_{eWG} - T_{eCDIP}$) plotted against $u_{ob}\cos(\theta_{r_{T_e}})$
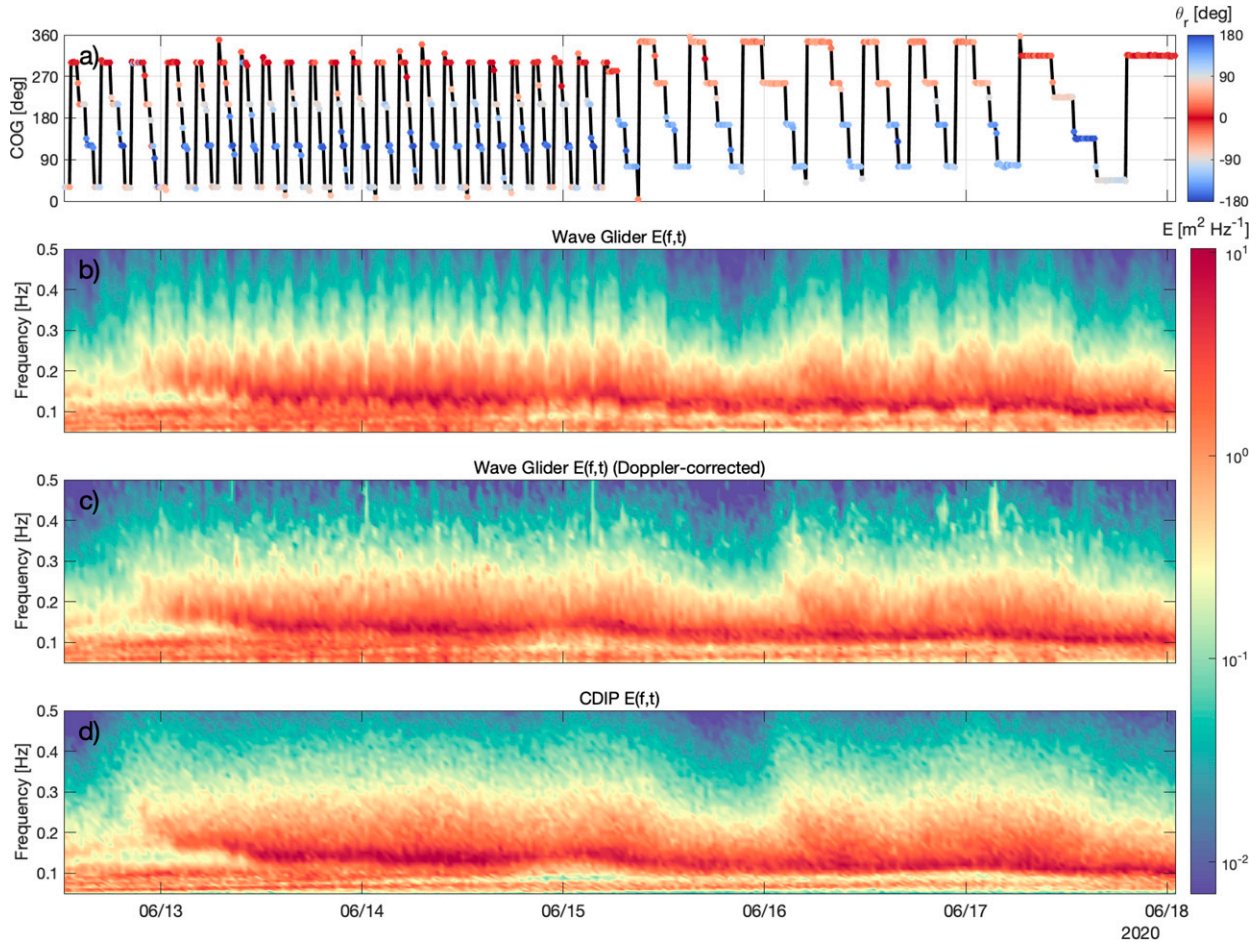
FIG. 4. (a) Vehicle course over ground (COG) and energy density spectrograms for (b) Wave Glider observed, (c) Wave Glider Doppler-corrected (using Wave Glider–based θ_r), and (d) CDIP observed wave spectra gathered during the San Nicolas Island experiment (067). Red and blue tones in (a) illustrate the wave encounter angle (θ_r) for head and following seas, respectively. The color in (b)–(d) is scaled to the log of the energy density.

(i.e., the vehicle's velocity projected along the axis of wave propagation) (Fig. 5). Here, the wave encounter angle ($\theta_{r_{T_e}}$) is computed as the difference between the vehicle's course over ground and the mean wave direction at the energy-weighted period T_e. We can derive a theoretical formulation for Doppler-induced ΔT in monochromatic waves by substituting $f = 1/T$ in Eq. (11) and solving for the difference between observed (T_{ob}) and intrinsic (T_{in}) wave periods

$$\Delta T = T_{ob} - T_{in} = -\frac{T_{in} 2\pi u_{ob}\cos(\theta_{r_{T_{in}}})}{g T_{in} + 2\pi u_{ob}\cos(\theta_{r_{T_{in}}})}, \qquad (18)$$

where the wave encounter angle, $\theta_{r_{T_{in}}}$, is defined at the intrinsic wave period. Expected ΔT values are shown in Fig. 5 (colored dashed lines) over a range of intrinsic wave periods and vehicle velocities [$u_{ob}\cos(\theta_{r_{T_{in}}})$] along with observed differences in energy-weighted period (ΔT_e).

Considering Doppler effects and the range of Wave Glider velocities (± 1.5 m s^{-1}), we anticipate ΔT_e to be inversely related to $u_{ob}\cos(\theta_r)$, as seen from Eq. (18) and Fig. 4 (dashed lines).

Moreover, a more pronounced ΔT response can be expected for shorter wave periods and higher relative vehicle speeds, though this effect is rather subtle for the parameter space presented in Fig. 5. Note also that the predicted ΔT response is asymmetric about zero, with greater |ΔT| values for following seas than for head seas at opposite relative velocities. To help build some intuition, we consider here two limiting cases. First, as the vehicle approaches the wave phase speed (c) in following seas [$u_{ob}\cos(\theta_r) \to -c$], $\Delta T \to \infty$ because the vehicle's relative velocity precludes it from experiencing the passage of waves. Second, the observed period decreases for increasing vehicle speeds in head seas or when the vehicle speed is greater than the phase speed in following seas (i.e., vehicle overtaking waves), such that as $u_{ob}\cos(\theta_r) \to \pm\infty$, $T_{ob} \to 0$, and $\Delta T \to -T_{in}$. Hence, a steeper ΔT gradient is expected in the following seas regime $-c < u_{ob}\cos(\theta_r) < 0$ when compared to opposite head seas velocities.

Results in Fig. 5 confirm that the predicted Doppler effects broadly reproduce the observed behavior, indicating that Doppler adjustments can account for vehicle motion reasonably well
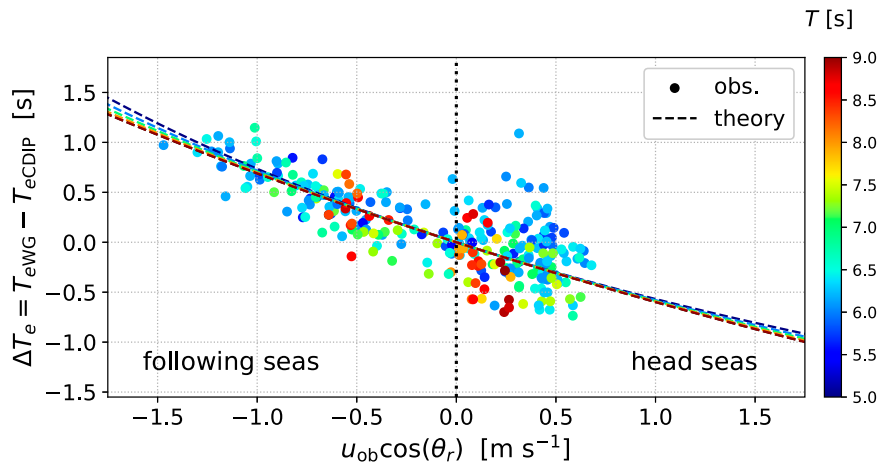
FIG. 5. Observed difference in energy-weighted period (ΔT_e) between the Wave Glider and the San Nicolas Island buoy as a function of vehicle velocity projected along the direction of wave propagation [$u_{ob}\cos(\theta_{r_{T_e}})$]. Colored dashed lines derived from (18) show expected ΔT values over a range of vehicle velocities and intrinsic wave periods. Colors illustrate the instantaneous T_e values observed by the buoy and corresponding intrinsic wave periods for the theoretical results (dashed lines).

(explaining over 60% of the observed ΔT_e variance in this case). For the present case, a mean southward current of ~ 0.25 m s^{-1} was measured at depths above the sub by the onboard ADCP. Average zonal currents were <1 cm s^{-1} during the observational period. This southward flow induced slower and faster vehicle speeds for reciprocal transects in head and following seas, respectively, as evidenced by the resulting velocity asymmetry seen in Fig. 5 (circles). To further illustrate the effectiveness of Doppler corrections, we apply them to Wave Glider spectra at each frequency using (13) and (14), assuming a constant vehicle speed and wave encounter angle for each time interval. A qualitative comparison of the Doppler-corrected spectrogram (Fig. 4c) with the control dataset (Fig. 4d) demonstrates that Doppler adjustments significantly diminish the frequency modulations arising from the vehicle's relative motion with respect to the wave field.

Several factors may explain the residual ΔT_e variations [i.e., those not captured by (18)] in Fig. 5, including spectral uncertainties (e.g., Drazen et al. 2016), statistical uncertainties associated with record length, and natural spatial variability in the wave field (e.g., Gemmrich et al. 2016). It is important to note that ΔT [Eq. (18)] and ΔT_e represent somewhat different quantities. The former is defined for monochromatic waves, whereas the latter is determined from observed spectra, which were generally broad banded throughout the observational period. Given that directional spreading is inherent to any realistic wave field, additional uncertainty arises from the estimation of θ and the subsequent calculation of θ_r. The assumption of constant vehicle speed embedded in the Doppler corrections and the effects of directional spreading are further discussed in section 5b.

2) WAVE DIRECTION

In this section, we contrast the Wave Glider directional wave measurements with those obtained by CDIP buoys at Torrey Pines Outer (CDIP 100 and NDBC 46225) and the San Nicolas Island (CDIP 067 and NDBC 46219) during the May and June 2020 evaluation experiments (datasets 100a and 067 in Table 2). These observations highlight the fidelity and limitations of the Wave Glider directional measurements in markedly different sea states. Specifically, waves at Torrey Pines Outer (100a) were generally narrow banded and dominated by long-period south-southwest swell (Figs. 6a,c,i) with $0.6 < H_s < 1.8$ m; a weakly bimodal spectral distribution, likely driven by the diurnal sea breeze, can also be observed over the last two days of the evaluation period (Fig. 6i). By contrast, the San Nicolas Island dataset (067) was dominated by broadbanded short-period wind seas out of the northwest with $1.1 < H_s < 3.2$ m for most of the observational period (Figs. 6b,d,j). Vehicle-based directional measurements [$\theta(f)$, obtained from (9)] were Doppler-corrected using procedures discussed in section 3d, and postprocessed to match CDIP's time base and frequency bands.

The main features of the Wave Glider mean wave direction estimates (Figs. 6a,b) are in close agreement with the corresponding CDIP observations (Figs. 6c,d) over a variety of sea states and wave encounter angles. Absolute angle differences ($|\Delta\theta|$) between the Wave Glider and CDIP directional measurements reveal regions of excellent agreement at energetic frequencies, while simultaneously highlighting discrepancies where wave energy is low (Figs. 6e,f,i,j). This can be seen more clearly in Fig. 7a, which shows the distribution of E as a function of $|\Delta\theta|$. At high energies, $|\Delta\theta|$ is always small (<15°); however, the number of values showing high directional discrepancies sharply increases for sufficiently low E values, suggesting that the observed deviations could be caused by insufficient signal-to-noise ratios. For example, around one-third of observations have $|\Delta\theta| > 15°$ for $E < 1$ m^2 Hz^{-1}. Not surprisingly, these high $|\Delta\theta|$ values also coincide with elevated levels of directional spreading, as shown in Fig. 7b.
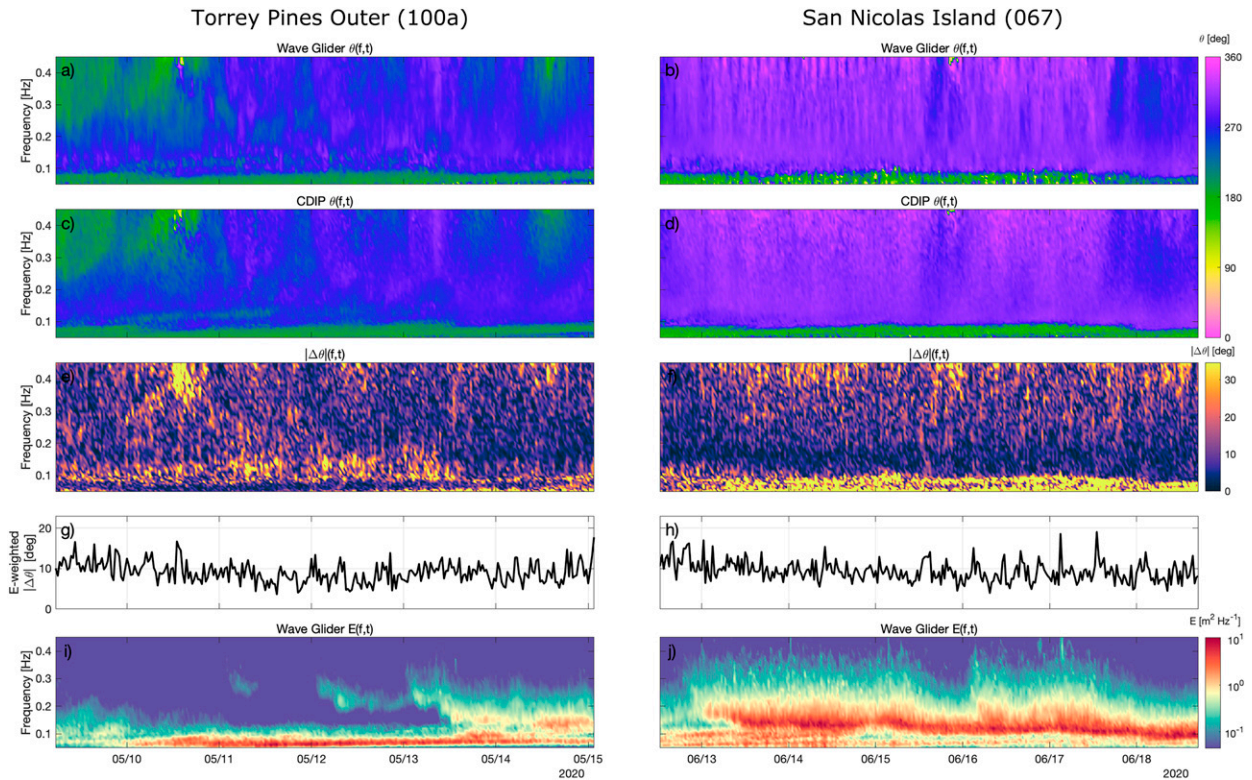
FIG. 6. Frequency-dependent mean wave direction (θ) from (9) for the (a),(b) Wave Glider and (c),(d) CDIP Waverider buoy at (left) the Torrey Pines and (right) the San Nicolas Island study sites. (e),(f) Absolute angle differences ($|\Delta\theta|$), (g),(h) energy-weighted $|\Delta\theta|$, and (i),(j) Wave Glider–based sea surface spectra (E) are presented. The color in (i) and (j) is scaled to the log of the energy density.

Energy-weighted absolute angle differences (Figs. 6g,h) are on average $<10°$ for both datasets and do not exhibit an obvious dependence on vehicle heading. Taken together, these results indicate that Wave Gliders can accurately resolve $\theta(f)$ at energetic frequencies regardless of sea state conditions and wave encounter angle.

3) BULK WAVE PARAMETERS

Scatterplots in Fig. 8 compare the Wave Glider measurements of H_s, T_e, and θ_e versus CDIP reference data. For both platforms, bulk wave parameters were computed from Doppler-corrected spectral estimates using Eqs. (15)–(17). Here, we consider data from all evaluation experiments (Table 2), which amounts to approximately 26 days of observations. RMSE and bias errors, computed from differences between Wave Glider and CDIP data following the procedures outlined in section 2d, are presented in Table 3. The resulting error metrics can be compared to the reported NDBC (2009) accuracies and the WMO (2018) operational requirements, also listed in Table 3 for reference. Least squares linear regression slopes and intercept values are shown in Fig. 8 for each of the observed variables together with the coefficient of determination (r^2). The reported r^2 values are derived from observational data.

Wave Glider estimates of significant wave height (H_s), energy-weighted period (T_e), and direction (θ_e) show strong quantitative agreement with the control data (Fig. 8), with typical errors comparable to those reported by the NDBC and that are well within the operational standards required by the WMO (Table 3). For the largest waves ($H_s > 2$ m) (Fig. 8a), the Wave Glider estimates of H_s show a small negative bias of -0.07 m or 3% (further discussion to follow in section 5c). No appreciable biases were detected between the Wave Glider and the DWR buoys in terms of T_e and θ_e, but higher T_e variability is observed for case 100b in longer period sea states (Fig. 8b). Error metrics for θ_e (Table 3) are consistent with those shown in Figs. 6g and 6h, and generally similar across all wave encounter angles and deployments (Fig. 8c). For T_e, Doppler adjustments reduced RMSE values by 37%, correcting bias errors greater than 1 s in some cases. Note that neither the calculation of H_s nor θ_e is influenced by Doppler shifting. This is because Doppler effects modulate the frequency mapping of E and θ but preserve the total spectral energy. Finally, we note that comparisons between the Wave Glider and CDIP yielded RMSE values of 2.0 s and 27.0° for peak period (T_p) and peak direction (θ_p), respectively.

4. Current measurements

a. ADCP configuration and data processing

Wave Gliders were outfitted with a downward-looking 300-kHz Teledyne RDI Workhorse Monitor ADCP, installed in the aft
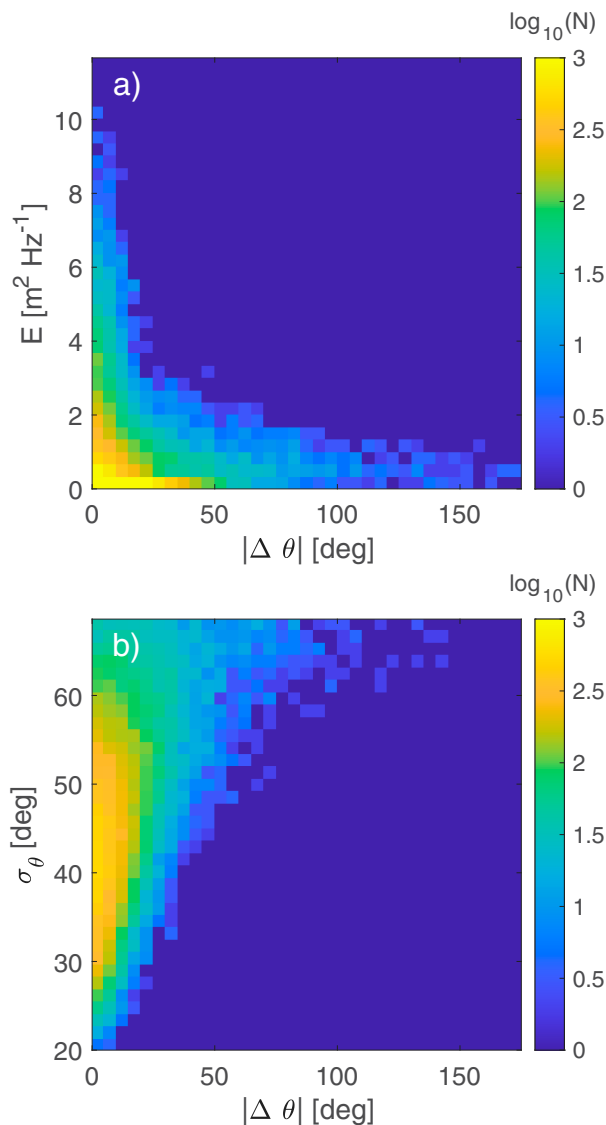
FIG. 7. Histograms of (a) sea surface energy (E) and (b) wave directional spread (σ_θ) vs absolute angle differences ($|\Delta\theta|$). Colors illustrate the data distribution as $\log_{10}(N)$, where N represents the number of values. Histograms are based on Wave Glider data from the 100a and 067 datasets (Table 2).

payload bay of the float. The Workhorse Monitor employs four separate transducers oriented in a Janus configuration, with beams pointing at a 20° angle with respect to the vertical. ADCP transducers are mounted through the float's hull with beam 3 oriented 135° counterclockwise from the float's bow. The onboard ADCP is powered by the vehicle's electrical system and controlled by the SMC. Raw ADCP and ancillary (i.e., GPS, internal magnetic compass, and internal tilt sensor) data are stored locally on the SMC and transmitted to shore via either cell or Iridium Router-based Unrestricted Digital Internetworking Connectivity Solution (RUDICS) using onboard modems. Wave Glider ADCPs were configured to sample continuously at 1 Hz using 2-m bins and a blanking distance

of 1.8 m, reliably measuring current profiles down to a depth of approximately 80 m.

Raw ADCP data were collected in beam coordinates, imported into MATLAB (rdradcp.m developed by Rich Pawlowicz, https://www.eoas.ubc.ca/~rich/#RDADCP), and postprocessed as follows. First, water velocity profiles (relative to the instrument) are computed via the standard ADCP beam-to-instrument coordinate transformation. These apparent velocities are subsequently rotated into a stable north–east–down (NED) coordinate system using the instantaneous pitch, roll, and heading angles recorded by the ADCP's ancillary sensors. Note that the instrument's internal magnetic compass requires a correction for local magnetic declination. To determine water velocity profiles in an Earth-fixed reference frame, the vehicle's translational motion is added to the apparent current. These translational velocities are obtained by differentiating the Wave Glider's GPS positions over a 90-s interval of travel. A basis for selecting this motion compensation time window is provided in section 4c(1).

To ensure data quality, ADCP velocity pings were carefully screened at each depth level. Along-beam velocities were rejected for instrument tilts greater than ±20°, and for beam correlations and intensities below 90 and 60 counts, respectively. Single-ping velocity data were also rejected when ADCP error velocities exceeded 10 cm s^{-1}. To avoid acoustic contamination by sidelobe reflections, velocity data near the seabed (around 7% of range to boundary) were masked. Acoustic reflections from the Wave Glider sub (Fig. 2) also limit the reliability of the onboard ADCP data at the sub's depth and at the first harmonic depth (8 and 16 m), as noted by Grare et al. (2021). Velocity measurements corresponding to these compromised depth cells were therefore removed and linearly interpolated using data from neighboring bins. The Wave Glider velocity data were temporally averaged into 15-min (900 pings) ensembles to match those reported by the Del Mar mooring (see next section). Velocity ensembles were discarded when the fraction of rejected single ping data exceeded 40% of the record.

b. ADCP evaluation datasets

Three Wave Glider surveys were conducted near the Del Mar mooring (Fig. 1c; http://mooring.ucsd.edu/delmar1/) during the spring, summer, and fall of 2021 to characterize the measurement accuracy of the onboard ADCP relative to a fixed asset. The location of the evaluation site and the bathymetry of the survey region are illustrated in Fig. 1j along with the corresponding Wave Glider tracks. The Wave Gliders were programmed to sustain box-shaped surveys centered about the mooring location with legs of size 800–1200 m, depending on the survey (Table 4). An overview of the datasets is presented in Table 4.

The Del Mar mooring is a long-term monitoring station located on the shelf break at the 100-m isobath (32.929°N, 117.317°W), approximately 5.2 km offshore of Torrey Pines State Beach. Isobaths at the mooring site are oriented about 12° counterclockwise from true north and roughly aligned with the coastline (Fig. 1j). The mooring and its surface buoy are outfitted with a suite of meteorological and oceanographic sensors, including a sonic anemometer, nine CTD sensors,
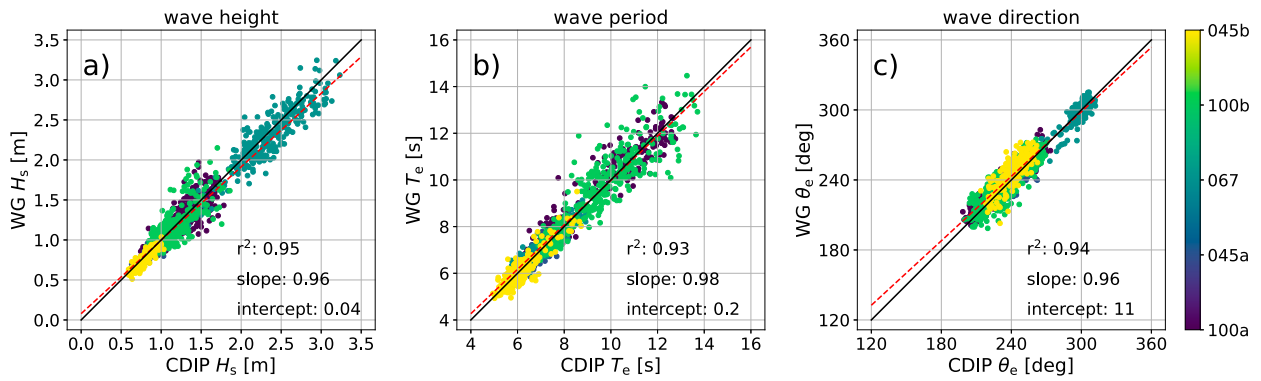
FIG. 8. Scatterplot comparisons of (a) significant wave height, (b) energy-weighted wave period, and (c) energy-weighted wave direction. Color-coded circles indicate the associated wave evaluation experiment (Table 2). Black lines represent one-to-one relationships; red dashed lines illustrate linear regression results with corresponding slope and intercept values annotated; r^2 values are calculated from observational data.

and a downward-looking four-beam 300-kHz RD Instruments Workhorse ADCP. The latter is configured to sample water velocities in 2-m bins starting 5.4 m below the sea surface, and reports near-real-time data in 15-min bursts.

Currents at Del Mar mooring are predominantly along isobath, with low-frequency velocity variances that are roughly twice as large as those associated with tidal band motions (Winant and Bratkovich 1981). Alongshore currents respond to a variety of atmospheric and oceanographic phenomena (e.g., large-scale wind stress events, coastally trapped waves, and coastal eddies), and typically exhibit a dominant barotropic or mode-1 vertical structure (Hamann et al. 2021). Cross-shore currents, on the other hand, are mainly driven by tidal forcing and are dominated by a baroclinic vertical structure (i.e., a principal mode of variability that reverses with depth) when stratification is strong (Winant and Bratkovich 1981). During the comparison surveys, depth-averaged current velocity magnitudes of up to 0.25 m s^{-1} were observed. Conditions were characterized by moderate diurnal winds (of order 1–5 m s^{-1}) and strong vertical stratification for all experiments. Wave heights ranged between 0.5 and 1.0 m for both the spring and summer datasets. A larger northwest swell dominated the fall evaluation period, with significant wave heights ranging up to 2.25 m.

c. Evaluation of ADCP measurements

1) MOTION COMPENSATION

We compare GPS velocities (calculated from differentiated position) to the ADCP's bottom-tracking system to determine an optimal time window Δt for motion compensation. Ideally, Δt should be minimized so as to maximize the temporal resolution of the water velocity measurements. However, GPS velocities are limited by the absolute accuracy of the GPS receiver which in turn restricts our ability to resolve vehicle motions, especially when the distance between successive points ΔL is small. Bottom tracking, on the other hand, has a typical single-ping accuracy of a few millimeters per second, and has been demonstrated to provide very accurate estimates of vessel speed (e.g., Fong and Monismith 2004). An additional advantage of bottom tracking is that vehicle velocities and water velocity profiles are measured in the same coordinate system; hence, motion compensation is independent of the ADCP coordinate rotation or internal compass errors (Huang 2019). We emphasize, however, that bottom tracking is usually unavailable for Wave Gliders since they typically operate at depths that are beyond the range of most ADCPs (bottom-tracking range is about 1.5 times the water profiling range). It is also worth noting that bottom tracking slightly degrades the quality of the water pings (Firing and Hummon 2010).

To generate data for comparison with GPS-derived velocity estimates, bottom-tracking mode was enabled for a fraction of the spring 2021 deployment (Table 4). Along-track GPS velocities were determined by computing the distance between consecutive points and dividing that distance by Δt (i.e., the time elapsed between the positions), which ranged from 10 to 300 s. The bottom-track velocities were ensemble averaged in a NED reference frame over the time interval Δt and subsequently rotated into along- and cross-track components for each transect.

TABLE 3. System accuracies and WMO (2008) operational requirements for the observed wave variables. Overall comparisons are based on ~26 days of observations.

Measurement	RMSE	Bias	NDBC reported accuracy	WMO requirement
Wave height (m)	0.13	−0.02	0.20	0.50
Wave period (s)	0.53	0.04	1.0	1.0
Wave direction (°)	7.7	1.1	10	10

TABLE 4. Overview of ADCP evaluation datasets at Del Mar Mooring.

Survey	Dates	Wave Glider	Duration (days)
Spring 2021	31 Mar–1 Apr	Magnus	1.1
Summer 2021	26 Jul–4 Aug	SV3-1101	9.1
Fall 2021	26–28 Oct	Magnus	2.2

Positional uncertainties (of order 1 m) imply that GPS velocity errors should diminish with increasing distance ΔL. For relatively constant speeds, GPS velocity errors should similarly decrease with greater Δt values, as increasing ΔL requires Δt to increase as well. Ensemble averaging reduces the single-ping uncertainty of bottom tracking by a factor of $N^{-1/2}$, where N is the number of measurements in the bottom-tracking ensemble. Assuming a single-ping error on the order of 1 cm s^{-1} and considering that $10 < \Delta t < 300$ s, bottom-tracking uncertainties are thus expected to range between 10^{-2} and 10^{-4} m s^{-1}, resulting in a negligible contribution to the total uncertainty at higher Δt (for additional details see appendix, section a).

Figure 9a shows the RMSE between along-track GPS and bottom-track velocities as a function of time interval Δt, or equivalently, the average transect length ΔL. As expected, deviations initially decay sharply with increasing Δt values due to a corresponding decrease in both GPS-derived velocity and bottom-tracking errors. A broadening of the RMSE confidence intervals is observed as the number of transects available for comparison decreases with Δt, resulting in higher statistical uncertainty for greater Δt values. Note also that the RMSE approaches a constant value of about 3 cm s^{-1}, indicating a "minimum error" that is unaccounted for by GPS or bottom-tracking uncertainties. This constant minimum error is independent of Δt and may be related to ADCP compass heading errors. We estimate that heading errors are about 3.4° for the average vehicle speed of 0.50 m s^{-1} following the approach of Fong and Monismith (2004) (see appendix, section b). It is worth noting that these heading errors represent a bulk estimate of the compass deviations inferred from multiple transects with different orientations. Based on these results, we choose $\Delta t = 90$ s as our motion correction time scale as it provides a 95% reduction in Δt dependent velocity errors. The resulting GPS velocities show excellent agreement with their bottom-tracking counterparts over a wide range of values (Fig. 9b).

2) WATER VELOCITIES

In this section, we compare Wave Glider ADCP observations to measurements collected by the Del Mar Mooring. We first focus on data from the summer 2021 observational period (Table 4) to evaluate the quality and utility of the Wave Glider measurements. This dataset was selected because it comprises 73% of the available Wave Glider ADCP data, constituting our longest continuous record. We then draw on all datasets to provide a detailed look at systematic errors and overall accuracy. It is worth noting that, in contrast to wind and wave measurements, there are currently no formal WMO requirements for the accuracy of ocean current measurements. As
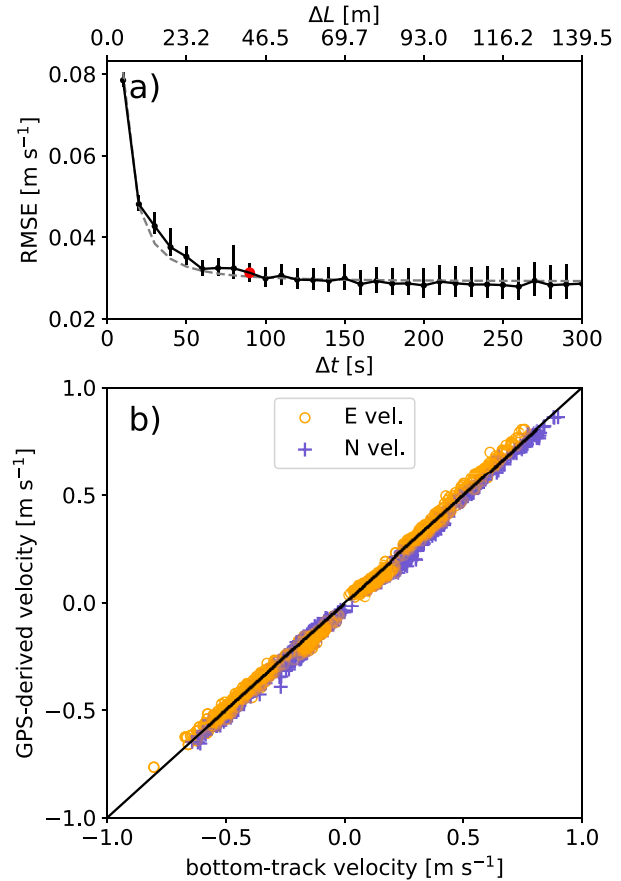

FIG. 9. (a) RMSE of along-track GPS-derived velocity estimates and ADCP bottom-track velocities as a function of time interval Δt (see also equivalent average transect length ΔL in top axis). (b) Scatterplot comparisons of GPS velocities vs bottom-track velocities for east (orange circles) and north (purple crosses) velocity components with $\Delta t = 90$ s [see red circle in (a)]. Error bars in (a) indicate the 95% confidence levels from bootstrapping and the dashed gray line shows the best-fit error model (A1) output assuming a single ping error of 1 cm s^{-1} (see appendix). The black line in (b) corresponds to a one-to-one relationship.

noted in section 4a, the higher temporally resolved Wave Glider observations are motion compensated and time averaged into 15-min ensembles to match the Del Mar Mooring's time base. Velocity profiles from the mooring are vertically interpolated to match the vehicle's ADCP depth bins. To avoid spurious return signals from the sub, Wave Glider measurements from the 8- and 16-m-depth bins are replaced with the mean of neighboring bins. An evaluation of the resulting water velocities is presented below.

Figure 10 illustrates ADCP velocity measurements collected by the Wave Glider (top panels) and the Del Mar Mooring (bottom panels) during the summer 2021 comparison period (Table 4). While there are subtle differences in the velocity estimates, the Wave Glider observations show close qualitative agreement with those of the mooring for both northward (alongshore) and eastward (cross-shore) velocity components,
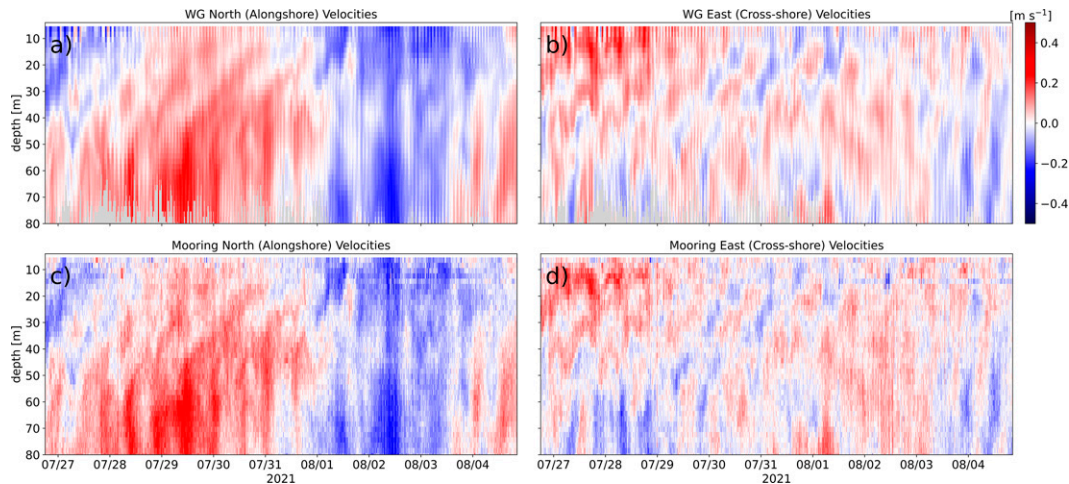
FIG. 10. Velocity measurements gathered during the summer 2021 deployment by ADCPs mounted on (a),(b) the Wave Glider and (c),(d) the Del Mar Mooring. Warmer (red) and cooler (blue) colors indicate northward and southward flows in (a) and (c), respectively, and eastward and westward flows in (b) and (d). Data that do not meet the screening requirements (section 4a) are masked in gray. All plots share the same color bar.

capturing key features in the vertical structure and temporal evolution of the currents. For example, both measurement systems show a surface-intensified southeastward flow during the initial phase of the evaluation period, between 26 and 29 July, with an opposing northward current at depth. After this event, strong subtidal alongshore currents are observed with significantly weaker cross-shore velocities. Measurements from both platforms exhibit a dominant barotropic vertical structure for the alongshore currents (Figs. 10a,c, 11a), as reported by previous observational studies conducted at Del Mar (Winant and Bratkovich 1981; Hamann et al. 2021). By contrast, the cross-shore currents often feature one or more zero crossings throughout the water column (Figs. 10b,d). Spectral analysis indicates that these cross-shore velocity fluctuations are significantly coherent with the density signal at tidal and higher frequencies with maximum coherence ($Coh^2 = 0.84$) at the semidiurnal frequency, suggesting a correspondence with the shoaling internal tide.

To further examine the utility of the Wave Glider ADCP measurements, we inspect the three leading empirical orthogonal function (EOF) modes of the alongshore velocity component (Figs. 11a–c) and the associated velocity amplitudes (Figs. 11d–f). The leading EOF modes explain 83.8%, 8.1%, and 2.6% of the total variance for the Wave Glider observations, and 77.9%, 7.1%, and 2.6% for the mooring data. These results are broadly consistent with those obtained by Winant and Bratkovich (1981), who found that over 90% of the alongshore current variability at Del Mar can be accounted for by the first two eigenfunctions. Furthermore, vehicle-based velocity amplitudes (Figs. 11d–f) and vertical current structures (Figs. 11a–c) reproduce those of the mooring over most of the water column, indicating that the principal modes of flow variability can be accurately resolved by Wave Glider–based ADCP measurements. Slight discrepancies in the EOFs, however, can be observed, especially in the upper third of the water column. We explore the source of these deviations below.

To quantify the accuracy of the Wave Glider ADCP measurements, velocity profiles from both platforms were first rotated into the vehicle's along- and cross-track reference frame. Ensemble-averaged velocity differences ($\Delta V = V_{WG} - V_{DM}$) were then calculated using data from all surveys (Table 4), yielding over 1150 profiles in each axis. Though presumed contaminated (see section 4a), velocity differences at the 8- and 16-m-depth cells are shown in Fig. 12a (dashed lines) for reference.

Ensemble-averaged ΔV profiles (Fig. 12a) exhibit a negligible bias in the cross-track direction and a net velocity difference in the along-track direction centered at bins near the sub ($r_{sub} = 8$ m) and its first two harmonic depths ($2r_{sub}$ and $3r_{sub}$). This apparent forward (along-track) bias rapidly decays to 46% and 3% of its 8-m value for each successive harmonic (Fig. 12a, dashed blue lines), and while highly diminished, it is still detectable in bins immediately above and below the 8- and 16-m-depth cells. Further analysis of ΔV_{fwd} indicates that along-track biases increase with vehicle speed (Fig. 12b). Note, however, that the observed biases cannot be attributable to GPS velocity errors as this would lead to a bulk offset in the ΔV_{fwd} profile across the water column. As for the observed scatter (Fig. 12a, shaded regions), our results show that ensemble-averaged ΔV profiles produce approximately uniform RMSE values of ~3.5 cm s^{-1} for both axes at depths greater than ~$3r_{sub}$, consistent with the constant minimum error observed in the GPS versus bottom-tracking velocity comparisons (Fig. 9a). RMSE estimates increase above ~$3r_{sub}$ toward the surface to about 6 and 10 cm s^{-1}, respectively, for cross- and along-track velocity differences. This sudden increase in the RMSE is likely associated with the influence of sidelobe reflections from the sub, which are expected to interfere with the water velocity measurement. Not surprisingly, the RMSE values for ΔV_{fwd} are higher than those for ΔV_{stbd}; this is because the deviations for ΔV_{fwd} are susceptible to a forward bias that is modulated by vehicle speed variability.
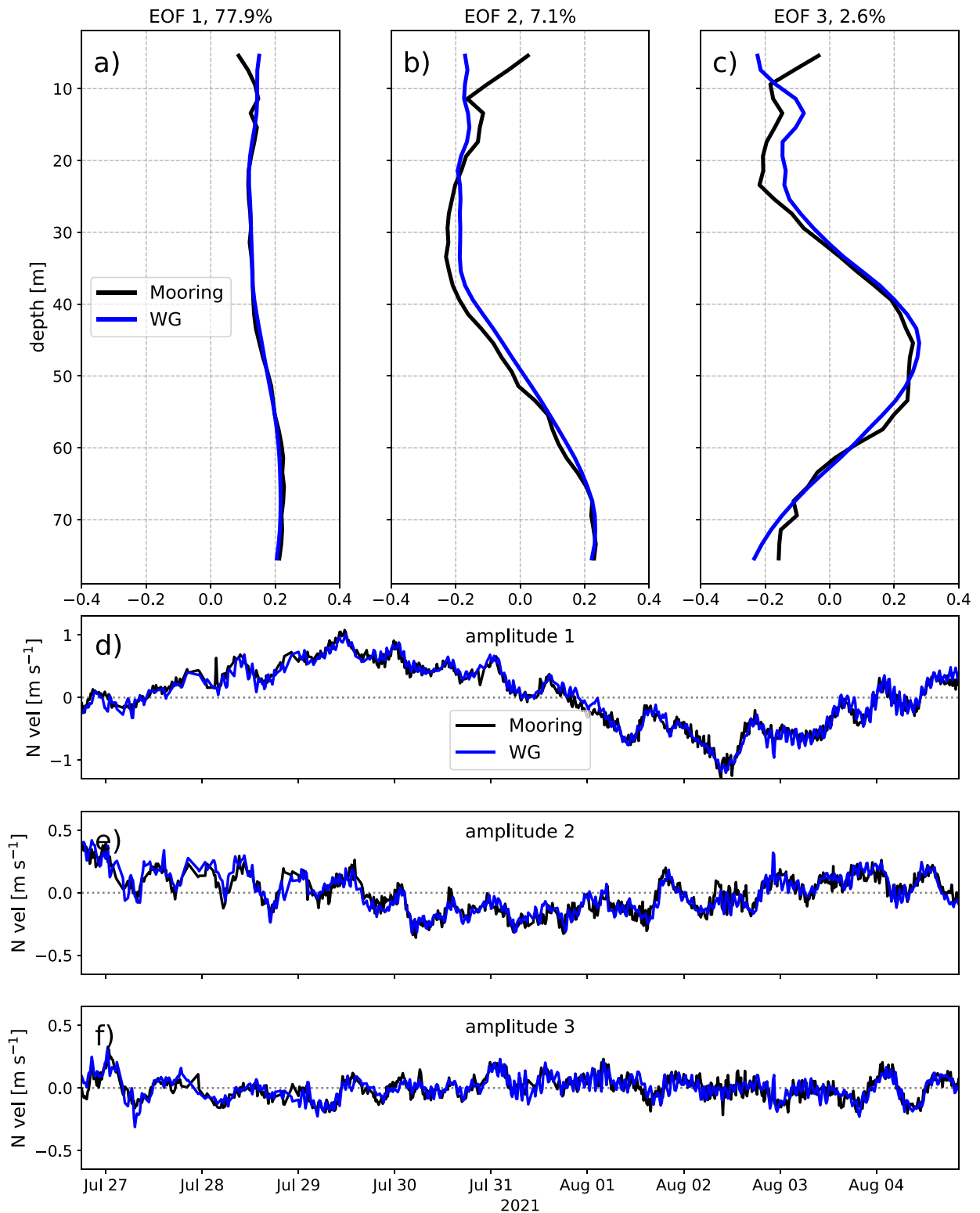
FIG. 11. (a)–(c) First three EOFs and (d)–(f) amplitudes of northward velocities calculated from Del Mar Mooring (black) and Wave Glider (blue) ADCP data collected during the summer 2021 deployment.
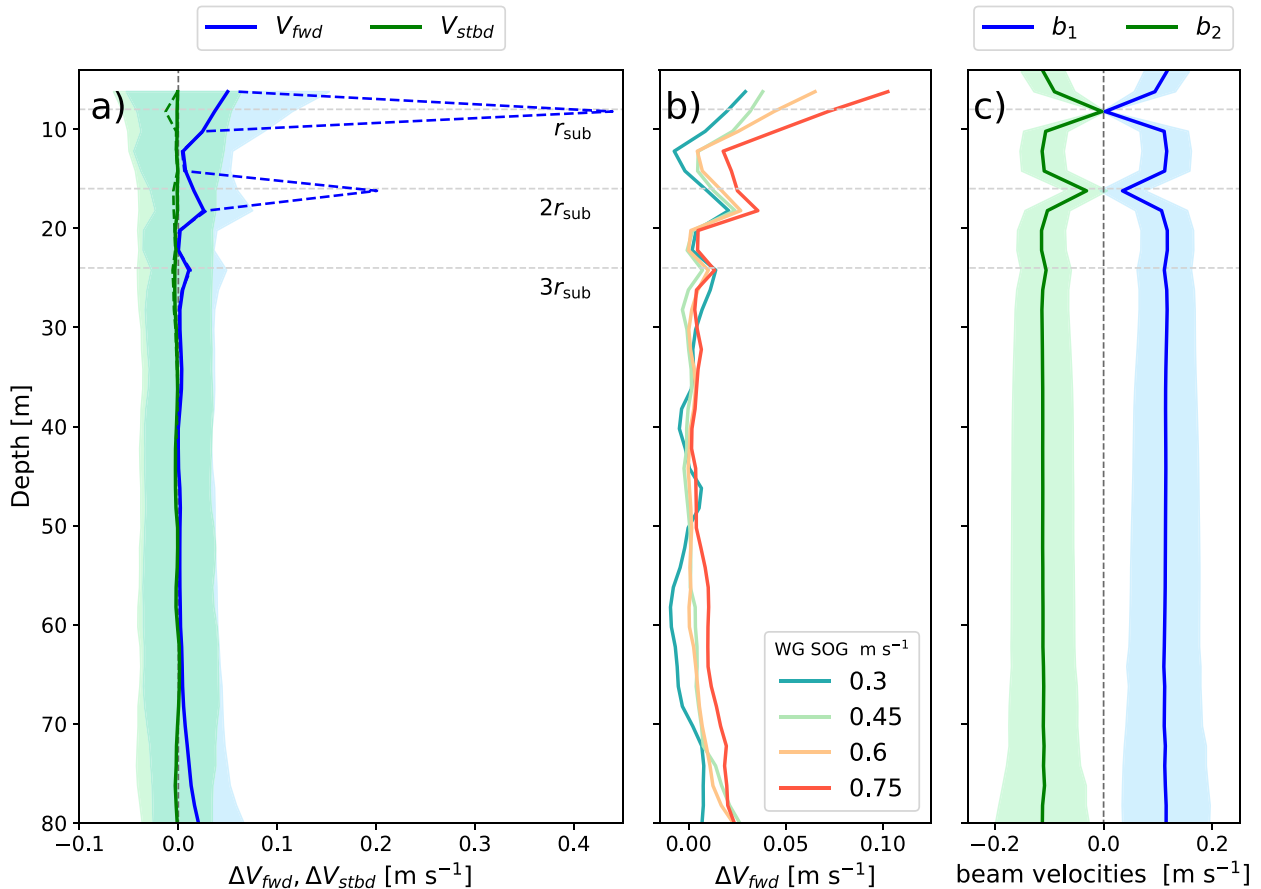
FIG. 12. (a) Along- (blue; ΔV_{fwd}) and cross-track (green; ΔV_{stbd}) ensemble-averaged velocity differences ($\Delta V = V_{WG} - V_{DM}$), considering all datasets listed in Table 4; (b) forward (along-track) residual velocities (ΔV_{fwd}) bin averaged for a range of along-track speed over ground (SOG) values; and (c) ensemble-averaged along-beam velocities for Wave Glider ADCP beams 1 (blue) and 2 (green). The shaded regions in (a) and (c) represent one standard deviation. The horizontal dashed gray lines indicate the depth of the sub ($r_{sub} = 8$ m) and its first two harmonics ($2r_{sub}$, $3r_{sub}$). Note that velocity differences (solid lines) at r_{sub} and $2r_{sub}$ in (a) and (b) result from Wave Glider velocities that have been replaced with the mean of adjacent bins. Though presumed contaminated (see section 4a), raw velocity differences at r_{sub} and $2r_{sub}$ are also shown in (a) for reference (dashed blue and green lines).

A more direct indication of acoustic contamination from the sub is presented in Fig. 12c. Inspection of ensemble-averaged along-beam velocity profiles for Wave Glider ADCP beams 1 and 2 reveals a bias toward zero at r_{sub}, with attenuated reverberations at $2r_{sub}$ and $3r_{sub}$. Beams 3 and 4 exhibit a similar vertical structure (not shown). Thus, the forward bias observed in Figs. 12a and 12b is simply a consequence of motion compensation (i.e., adding the Wave Glider velocity to the instrument-based velocities to arrive at Earth-based water velocities).

5. Discussion

a. Wave sheltering

Previous studies have suggested that low-elevation anemometers are prone to underestimating wind speeds, especially in the presence of large waves (Schmidt et al. 2017; Thomson et al. 2018). We emphasize, however, that the wind comparisons here are limited to moderate to rough sea states with $1 < H_s < 3.5$ m and $6 < T_p < 21$ s, and wind speeds below 13 m s^{-1}. Recent work by Donelan (2018) suggests that wave sheltering is not a prominent effect until the onset of airflow separation (from the crests of the dominant waves), which typically occurs at speeds well above 20 m s^{-1} on the open ocean. The lack of wave sheltering is therefore reasonable given the relatively low wind speeds observed. Thus, the present findings may not extend to more energetic or extreme environments like tropical cyclones (e.g., Lenain and Melville 2014; Mitarai and McWilliams 2016). Additional comparisons in high wind regimes and larger sea states are needed to assess the effects of wave sheltering and the resulting impacts on the Wave Glider bulk wind observations. Alternatively, wind observations could be conditionally averaged by wave phase to identify the presence of wave sheltering, even if the impact on mean winds is small.

b. Applicability of Doppler corrections

The results in Figs. 4 and 5 offer compelling evidence to support the idea that Doppler corrections [Eqs. (13) and (14)] are applicable for the Wave Glider despite the propulsive nature of the platform. The key here is that the wave-driven propulsion system generates forward thrust as the sub moves up and down in the water column, with reasonably short transient periods (Rampersadh 2018). While the float tracks the wave orbitals at the free surface, it is simultaneously being towed by the sub at a reasonably steady velocity when traveling along a straight path. This is especially the case when the vehicle travels in favor of currents. Analysis and results by Amador et al. (2021) indicate that along-track currents provide a significant contribution to the Wave Glider's speed. It follows that the vehicle's translational velocity tends to be more constant for faster speeds, which is also when Doppler shifting becomes more pronounced. The assumption of constant speed is therefore justified in most cases, so long as the vehicle does not turn.

Also, it is important to bear in mind that the Doppler correction technique described in this study derives the wave encounter angle (θ_r) from the mean wave direction (θ). This can lead to the erroneous projection of spectral energies onto θ from waves that propagate in directions other than the mean wave direction. An alternative approach would involve using the directional wave spectrum for Doppler corrections, thus allowing for variations in spectral energy as a function of wave direction. This, however, is beyond the scope of this study. Nevertheless, the validity of the Doppler correction technique proposed and applied here is clearly supported by the current findings; its application produced significant improvements to the Wave Glider measurements of wave spectra (Fig. 4), mean wave directions (Fig. 6), and wave periods [see section 3g(3)]. The approach developed can be generalized to other environmentally propelled ASVs.

c. The float's heave response

Results in Fig. 8 corroborate and extend the findings of prior studies (Grare et al. 2021; Lenain and Melville 2014; Thomson et al. 2018), confirming that robust estimates of bulk wave statistics can be obtained from the Wave Glider platform over a wide range of sea states. As noted, however, a slight negative H_s bias (-7 cm) is apparent in Fig. 8a for the largest waves ($H_s > 2$ m) observed at the San Nicolas Island study site (dataset 067 in Table 2), which was dominated by short-period wind waves for most of the observational period. This low bias could be associated with the vehicle's surface-following properties in energetic high-frequency waves. The calculation of H_s assumes that the Wave Glider float closely follows the vertical wave motions at the surface. In practice, however, the float's heave response will deviate from the actual wave motions for sufficiently high frequencies (e.g., Alvarez 2015; Thomson et al. 2015). For the 067 dataset, the vehicle spectra begin to slightly deviate from the buoy spectra at wavelengths smaller than around 25 m ($T \lesssim 4$ s), suggesting that the float's geometry and inertia could be partially attenuating the higher-frequency waves. All other datasets were mostly unaffected by the float's seemingly muted response because the attenuated frequencies had minimal energy. However, this heave response attenuation to short waves could complicate the measurement of the equilibrium and saturation ranges in the high-frequency tail of the wave spectra; this will be addressed in a future study.

d. ADCP bias

Despite providing accurate current measurements over most range cells, Wave Glider ADCPs exhibit substantial biases at the sub's depth (r_{sub}) and at subsequent harmonic depths due to acoustic contamination (Fig. 12). The apparent absence of along-beam velocities at r_{sub} (Fig. 12c) implies a zero Doppler shift in the return signal that can be explained by the lack of relative motion between the sub and the ADCP over the 15-min averaging interval. Even though acoustic energy is focused along the center of the beams (or main lobes), a small amount of energy radiates out in undesired directions via acoustic sidelobes. Since ADCP beams are slanted, the sidelobes encounter the sub before the main lobe. These sidelobe reflections can easily overwhelm the acoustic return signal from r_{sub} because the sub provides much stronger reflections than the small scatterers used by the ADCP to measure the water velocities. This results in a bias toward the zero-mean relative velocity of the sub.

As previously noted, the effects of acoustic contamination are also evident at the 16- and 24-m-depth cells (Fig. 12). We hypothesize that these attenuated reverberations below the sub arise from consecutive reflections between the sub and the sea surface, such that virtual image reflections of the sub appear at discrete intervals $r_i = n r_{sub}$, where r_i is the image range, r_{sub} is the sub's range (or depth), and n is given by positive integers ($n = 1, 2, 3 \ldots$). Furthermore, sidelobe reflections and acoustic scattering from the sub together with the time-varying amplitude of the sub's vertical excursions (relative to the float) are likely responsible for the remnant biases observed in bins adjacent to those at r_{sub} and $2r_{sub}$ (Fig. 12). Recent work by Lentz et al. (2022) indicates that, due to range gating, sidelobe contamination can extend to $z_{sl} + 3\Delta z/2$, where Δz is the ADCP bin size, $z_{sl} = r_{sub}[1 - \cos(\theta)]$ is the center depth of the sidelobe reflection, and θ is the ADCP beam angle from the vertical. For the present case $r_{sub} = 8$ m, $\Delta z = 2$ m, and $\theta = 20°$; the contaminated region can thus be expected to extend ~3.5 m from the sub, leading to an overlap between r_{sub} and neighboring depth bins.

The presence of the along-track bias at r_{sub} and $2r_{sub}$ has long been known, and is typically handled through the removal of the corresponding velocity data (e.g., Grare et al. 2021). The analysis in section 4c(2) reveals that remnant biases of several centimeters per second or about 10% of the vehicle's velocity are also present in bins adjacent to the sub, with attenuated reverberations at bins neighboring the $2r_{sub}$ depth cell. This result implies that measured currents at subadjacent depth bins (and potentially those neighboring $2r_{sub}$) may also need to be discarded in weak flows [$O(5)$ cm s^{-1}] since velocity biases could be comparable to, or even dominate, the current signal.

6. Concluding remarks

In this paper we have examined the quality of Wave Glider measurements and described methods for motion compensation. We have shown that Wave Gliders are capable of obtaining research-grade measurements of essential atmospheric and oceanographic variables via field comparisons against well-established moored buoy assets. Assessment of vehicle-based measurements of air temperature, barometric pressure, bulk winds, and bulk wave statistics indicates that Wave Gliders can reliably achieve WMO accuracy requirements, with error metrics (uncertainties and biases) that are comparable to those of operational NDBC buoys. This implies that Wave Glider observations are adequate for satellite-based sensor calibration and validation, and assimilation into weather, ocean, and climate models. The observations may also be used to provide climatological data in remote ocean areas. Finally, the mobility of ASVs provides new opportunities for adaptive sampling of temporally and spatially evolving environmental features of interest.

Data availability statement. Tanner Bank buoy data are openly available from NDBC (https://www.ndbc.noaa.gov/station_history.php?station=46047). Data from the Del Mar mooring are available by the Ocean Time Series Lab at SIO (http://mooring.ucsd.edu/delmar1/delmar1_16/nc/and and http://mooring.ucsd.edu/delmar1/delmar1_17/nc/). Reference wave data are openly available from CDIP (https://thredds.cdip.ucsd.edu/thredds/catalog/cdip/realtime/catalog.html). The Wave Glider data are available online as part of the UC San Diego Library Digital Collections (https://doi.org/10.6075/J0P26Z97).

APPENDIX

Vehicle Velocity and Compass Heading Errors

a. Expected vehicle velocity errors

The present analysis compares GPS-derived velocities to the ADCP bottom-tracking system in an Earth-based reference frame. Here, we assume that bottom tracking, GPS, and compass heading uncertainties comprise the main sources of error. We therefore represent the total vehicle velocity errors as

$$\epsilon_T^2 = \epsilon_{BT}^2 + \epsilon_{GPS}^2 + \epsilon_C^2, \tag{A1}$$

where ϵ_{BT} are the bottom-tracking errors, ϵ_{GPS} are the GPS velocity errors, and ϵ_C represents an error that is independent of the time-averaging interval (Δt). We postulate that ϵ_C is likely the result of ADCP compass heading errors [section 4c(1)]. The bottom-tracking errors are given by

$$\epsilon_{BT}^2 = \frac{\epsilon_{sp}^2}{N}, \tag{A2}$$

where ϵ_{sp} is the single-ping error and N corresponds to the number of measurements in the ensemble (bottom-tracking system was configured to sample at 1 Hz). For a constant vehicle speed, the GPS velocity errors can be expressed as

$$\epsilon_{GPS}^2 = \left(\frac{\epsilon_x}{\Delta t}\right)^2, \tag{A3}$$

where ϵ_x is the absolute horizontal accuracy of the GPS receiver and Δt is our motion correction time interval. By assuming $\epsilon_{sp} = 1$ cm s^{-1} and fitting the total vehicle velocity error model [Eq. (A1)] to our data (Fig. 9a), we estimate $\epsilon_x \approx 0.75$ m and $\epsilon_C \approx 0.029$ m s^{-1}.

b. ADCP compass errors

A simple analysis is carried out to describe ADCP compass heading errors following the approach of Fong and Monismith (2004). Let u_i, v_i and u_{BT}, v_{BT} be the bottom-track velocities in the instrument and Earth reference frames, respectively. A set of transformation equations can be written

$$\begin{aligned} u_{BT} &= u_i \cos(\phi + \phi_\epsilon) - v_i \sin(\phi + \phi_\epsilon), \\ v_{BT} &= u_i \sin(\phi + \phi_\epsilon) + v_i \cos(\phi + \phi_\epsilon), \end{aligned} \tag{A4}$$

such that ϕ denotes the actual transformation angle (accounts for local magnetic declination) between the coordinate systems and ϕ_ϵ is a compass angle error. Using the addition laws for sines and cosines, the velocity components can be rewritten as

$$\begin{aligned} u_{BT} &= u_i\,(\cos\phi\cos\phi_\epsilon - \sin\phi\sin\phi_\epsilon) - v_i(\sin\phi\cos\phi_\epsilon + \cos\phi\sin\phi_\epsilon), \\ v_{BT} &= u_i\,(\sin\phi\cos\phi_\epsilon + \cos\phi\sin\phi_\epsilon) + v_i(\cos\phi\cos\phi_\epsilon - \sin\phi\sin\phi_\epsilon). \end{aligned} \tag{A5}$$

Assuming that $\phi_\epsilon \ll 1$, so that $\cos\phi_\epsilon \approx 1$ and $\sin\phi_\epsilon \approx \phi_\epsilon$, we obtain

$$\begin{aligned} u_{BT} &\approx u_i \cos\phi - v_i \sin\phi - \phi_\epsilon(u_i \sin\phi + v_i \cos\phi), \\ v_{BT} &\approx u_i \sin\phi + v_i \cos\phi + \phi_\epsilon(u_i \cos\phi - v_i \sin\phi), \end{aligned} \tag{A6}$$

and noting that the vehicle's actual (true) velocities are given by

$$\begin{aligned} u_T &= u_i \cos(\phi) - v_i \sin(\phi), \\ v_T &= u_i \sin(\phi) + v_i \cos(\phi), \end{aligned} \tag{A7}$$

we rewrite (A6) as

$$u_{\mathrm{BT}} \approx u_T - \phi_\epsilon v_T,$$
$$v_{\mathrm{BT}} \approx v_T + \phi_\epsilon u_T, \qquad (\mathrm{A8})$$

To estimate ϕ_ϵ, we compute the difference between bottom-tracking and GPS speeds. This yields

$$(u_{\mathrm{BT}}^2 + v_{\mathrm{BT}}^2) - (u_{\mathrm{GPS}}^2 + v_{\mathrm{GPS}}^2) = \epsilon_{\mathrm{BT}}^2 + \epsilon_{\mathrm{GPS}}^2 + \epsilon_C^2, \qquad (\mathrm{A9})$$

where u_{GPS} and v_{GPS} are, respectively, the GPS-derived east and north velocity components. Because GPS and bottom-tracking velocity errors are time dependent, we expect that $\epsilon_{\mathrm{GPS}} \to 0$ and $\epsilon_{\mathrm{BT}} \to 0$, and $u_{\mathrm{GPS}} \to u_T$ and $v_{\mathrm{GPS}} \to v_T$, as $\Delta t \to \infty$; thus using (A8), we rewrite (A9) as

$$(u_T^2 - 2\phi_\epsilon u_T v_T + \phi_\epsilon^2 v_T^2) + (v_T^2 + 2\phi_\epsilon u_T v_T + \phi_\epsilon^2 u_T^2)$$
$$- (u_T^2 + v_T^2) = \epsilon_C^2, \qquad (\mathrm{A10})$$

which reduces to

$$\phi_\epsilon^2(u_T^2 + v_T^2) = \epsilon_C^2. \qquad (\mathrm{A11})$$

Equation (A11) quantifies the compass heading error as a function of vehicle speed and Δt-independent errors. For an average vehicle speed $(u_T^2 + v_T^2)^{1/2} \approx 0.5 \ \mathrm{m \ s^{-1}}$ and $\epsilon_C \approx 0.029 \ \mathrm{m \ s^{-1}}$ (estimated in appendix, section a), we obtain $\phi_\epsilon \approx 0.06 \ \mathrm{rad} \approx 3.4°$.

REFERENCES

Alvarez, A., 2015: Assessment of sea wave spectra using a surfaced glider. *Deep-Sea Res. I*, **102**, 135–143, https://doi.org/10.1016/j.dsr.2015.04.015.

Amador, A., S. T. Merrifield, R. A. McCarthy, R. Young, and E. J. Terrill, 2021: Wave Glider speed model for real-time motion planning. *OCEANS 2021*, San Diego, CA, IEEE, https://doi.org/10.23919/OCEANS44145.2021.9705782.

Bograd, S. J., D. A. Checkley Jr., and W. S. Wooster, 2003: CalCOFI: A half century of physical, chemical, and biological research in the California Current System. *Deep-Sea Res. II*, **50**, 2349–2353, https://doi.org/10.1016/S0967-0645(03)00122-X.

Centurioni, L. R., and Coauthors, 2019: Global in situ observations of essential climate and ocean variables at the air–sea interface. *Front. Mar. Sci.*, **6**, 419, https://doi.org/10.3389/fmars.2019.00419.

Cifuentes-Lorenzen, A., J. B. Edson, C. J. Zappa, and L. Bariteau, 2013: A multisensor comparison of ocean wave frequency spectra from a research vessel during the Southern Ocean Gas Exchange Experiment. *J. Atmos. Oceanic Technol.*, **30**, 2907–2925, https://doi.org/10.1175/JTECH-D-12-00181.1.

Collins, C. O., III, 2012: In situ wave measurements: Sensor comparison and data analysis. M.S. thesis, Rosenstiel School of Marine and Atmospheric Science, University of Miami, 181 pp., https://scholarship.miami.edu/esploro/outputs/graduate/In-Situ-Wave-Measurements-Sensor-Comparison/991031447696402976.

——, and Coauthors, 2017: Doppler correction of wave frequency spectra measured by underway vessels. *J. Atmos. Oceanic Technol.*, **34**, 429–436, https://doi.org/10.1175/JTECH-D-16-0138.1.

Corredor, J. E., 2018: Platforms for coastal ocean observing. *Coastal Ocean Observing*, 1st ed. Springer, 67–84.

Cronin, M. F., and Coauthors, 2019: Air-sea fluxes with a focus on heat and momentum. *Front. Mar. Sci.*, **6**, 430, https://doi.org/10.3389/fmars.2019.00430.

D'Asaro, E. A., and Coauthors, 2018: Ocean convergence and the dispersion of flotsam. *Proc. Natl. Acad. Sci. USA*, **115**, 1162–1167, https://doi.org/10.1073/pnas.1718453115.

Delory, E., and J. Pearlman, 2018: *Challenges and Innovations in Ocean In Situ Sensors: Measuring Inner Ocean Processes and Health in the Digital Age.* Elsevier, 408 pp.

Donelan, M. A., 2018: On the decrease of the oceanic drag coefficient in high winds. *J. Geophys. Res. Oceans*, **123**, 1485–1501, https://doi.org/10.1002/2017JC013394.

Drazen, D., C. Merrill, S. Gregory, A. Fullerton, E. Terrill, and T. de Paolo, 2016: Interpretation of in-situ ocean environmental measurements. *Proc. 31st Symp. on Naval Hydrodynamics*, Monterey, CA, Office of Naval Research–Stanford University.

Drennan, W. M., M. Donelan, N. Madsen, K. B. Katsaros, E. A. Terray, and C. N. Flagg, 1994: Directional wave spectra from a swath ship at sea. *J. Atmos. Oceanic Technol.*, **11**, 1109–1116, https://doi.org/10.1175/1520-0426(1994)011<1109:DWSFAS>2.0.CO;2.

Edson, J. B., A. A. Hinton, K. E. Prada, J. E. Hare, and C. W. Fairall, 1998: Direct covariance flux estimates from mobile platforms at sea. *J. Atmos. Oceanic Technol.*, **15**, 547–562, https://doi.org/10.1175/1520-0426(1998)015<0547:DCFEFM>2.0.CO;2.

——, and Coauthors, 2007: The Coupled Boundary Layers and Air–Sea Transfer experiment in low winds. *Bull. Amer. Meteor. Soc.*, **88**, 341–356, https://doi.org/10.1175/BAMS-88-3-341.

——, and Coauthors, 2013: On the exchange of momentum over the open ocean. *J. Phys. Oceanogr.*, **43**, 1589–1610, https://doi.org/10.1175/JPO-D-12-0173.1.

Fairall, C. W., E. F. Bradley, J. E. Hare, A. A. Grachev, and J. B. Edson, 2003: Bulk parameterization of air–sea fluxes: Updates and verification for the COARE algorithm. *J. Climate*, **16**, 571–591, https://doi.org/10.1175/1520-0442(2003)016<0571:BPOASF>2.0.CO;2.

Firing, E., and J. Hummon, 2010: Shipboard ADCP measurements. The GO-SHIP repeat hydrography manual: A collection of expert reports and guidelines, IOCCP Rep. 14, https://www.go-ship.org/Manual/Firing_SADCP.pdf.

Fong, D. A., and S. G. Monismith, 2004: Evaluation of the accuracy of a ship-mounted, bottom-tracking ADCP in a nearshore coastal flow. *J. Atmos. Oceanic Technol.*, **21**, 1121–1128, https://doi.org/10.1175/1520-0426(2004)021<1121:EOTAOA>2.0.CO;2.

Gemmrich, J., J. Thomson, W. E. Rogers, A. Pleskachevsky, and S. Lehner, 2016: Spatial characteristics of ocean surface waves. *Ocean Dyn.*, **66**, 1025–1035, https://doi.org/10.1007/s10236-016-0967-6.

Gentemann, C. L., and Coauthors, 2020: Saildrone: Adaptively sampling the marine environment. *Bull. Amer. Meteor. Soc.*, **101**, E744–E762, https://doi.org/10.1175/BAMS-D-19-0015.1.

Ghani, M. H., L. R. Hole, I. Fer, V. H. Kourafalou, N. Wienders, H. Kang, K. Drushka, and D. Peddie, 2014: The SailBuoy remotely-controlled unmanned vessel: Measurements of near surface temperature, salinity and oxygen concentration in the northern Gulf of Mexico. *Methods Oceanogr.*, **10**, 104–121, https://doi.org/10.1016/j.mio.2014.08.001.

Grare, L., N. M. Statom, N. Pizzo, and L. Lenain, 2021: Instrumented Wave Gliders for air-sea interaction and upper ocean research. *Front. Mar. Sci.*, **8**, 664728, https://doi.org/10.3389/fmars.2021.664728.

Hamann, M. M., M. H. Alford, A. J. Lucas, A. F. Waterhouse, and G. Voet, 2021: Turbulence driven by reflected internal

tides in a supercritical submarine canyon. *J. Phys. Oceanogr.*, **51**, 591–609, https://doi.org/10.1175/JPO-D-20-0123.1.

Hanson, K. A., T. Hara, E. J. Bock, and A. B. Karachintsev, 1997: Estimation of directional surface wave spectra from a towed research catamaran. *J. Atmos. Oceanic Technol.*, **14**, 1467–1482, https://doi.org/10.1175/1520-0426(1997)014<1467:EODSWS>2.0.CO;2.

Hauser, D., K. Kahma, H. E. Krogstad, S. Lehner, J. A. J. Monbaliu, and L. R. Wyatt, Eds., 2005: Measuring and analysing the directional spectra of ocean waves. COST Rep., 465 pp.

Herbers, T. H. C., P. F. Jessen, T. T. Janssen, D. B. Colbert, and J. H. MacMahan, 2012: Observing ocean surface waves with GPS-tracked buoys. *J. Atmos. Oceanic Technol.*, **29**, 944–959, https://doi.org/10.1175/JTECH-D-11-00128.1.

Hine, R., and P. McGillivary, 2007: Wave-powered autonomous surface vessels as components of ocean observing systems. *20th Pacific Congress on Marine Science and Technology*, Honolulu, HI, PACON International, https://nsgl.gso.uri.edu/hawau/hawauc07001/001-HineRoger-WavePoweredAutonomous.pdf.

Hole, L. R., I. Fer, and D. Peddie, 2016: Directional wave measurements using an autonomous vessel. *Ocean Dyn.*, **66**, 1087–1098, https://doi.org/10.1007/s10236-016-0969-4.

Holthuijsen, L. H., 2010: *Waves in Oceanic and Coastal Waters*. Cambridge University Press, 404 pp.

Huang, H., 2019: The importance of ADCP alignment with GPS in moving-boat streamflow measurements. *Flow Meas. Instrum.*, **67**, 33–40, https://doi.org/10.1016/j.flowmeasinst.2019.04.002.

Johnston, P., and M. Poole, 2017: Marine surveillance capabilities of the AutoNaut wave-propelled unmanned surface vessel (USV). *OCEANS 2017*, Aberdeen, United Kingdom, IEEE, https://doi.org/10.1109/OCEANSE.2017.8084782.

Kohler, P. E. C., L. LeBlanc, and J. Elliott, 2015: SCOOP-NDBC's new ocean observing system. *OCEANS 2015*, Washington, DC, IEEE, https://doi.org/10.23919/OCEANS.2015.7401834.

Kuik, A. J., G. P. Van Vledder, and L. H. Holthuijsen, 1988: A method for the routine analysis of pitch-and-roll buoy wave data. *J. Phys. Oceanogr.*, **18**, 1020–1034, https://doi.org/10.1175/1520-0485(1988)018<1020:AMFTRA>2.0.CO;2.

Large, W. G., and S. Pond, 1981: Open ocean momentum flux measurements in moderate to strong winds. *J. Phys. Oceanogr.*, **11**, 324–336, https://doi.org/10.1175/1520-0485(1981)011<0324:OOMFMI>2.0.CO;2.

Lenain, L., and W. K. Melville, 2014: Autonomous surface vehicle measurements of the ocean's response to Tropical Cyclone Freda. *J. Atmos. Oceanic Technol.*, **31**, 2169–2190, https://doi.org/10.1175/JTECH-D-14-00012.1.

Lentz, S. J., A. Kirincich, and A. J. Plueddemann, 2022: A note on the depth of sidelobe contamination in acoustic Doppler current profiles. *J. Atmos. Oceanic Technol.*, **39**, 31–35, https://doi.org/10.1175/JTECH-D-21-0075.1.

Lindstrom, E., J. Gunn, A. Fischer, A. McCurdy, and L. K. Glover, 2012: A framework for ocean observing. UNESCO Rep. IOC/INF-1284 Rev.2, 28 pp., https://unesdoc.unesco.org/ark:/48223/pf0000211260.

Long, R. B., 1980: The statistical evaluation of directional spectrum estimates derived from pitch/roll buoy data. *J. Phys. Oceanogr.*, **10**, 944–952, https://doi.org/10.1175/1520-0485(1980)010<0944:TSEODS>2.0.CO;2.

Merrifield, S., and Coauthors, 2019: Autonomy system for USV/UUV coordinated sampling. *OCEANS 2019*, Seattle, WA, IEEE, https://doi.org/10.23919/OCEANS40490.2019.8962555.

Mitarai, S., and J. C. McWilliams, 2016: Wave Glider observations of surface winds and currents in the core of Typhoon Danas. *Geophys. Res. Lett.*, **43**, 11 312–11 319, https://doi.org/10.1002/2016GL071115.

Mullison, J., D. Symonds, and N. Trenaman, 2011: ADCP data collected from a liquid robotics Wave Glider. *2011 IEEE/OES 10th Current, Waves and Turbulence Measurements*, Monterey, CA, IEEE, 266–272, https://ieeexplore.ieee.org/document/5759563.

NDBC, 2009: Handbook of automated data quality control checks and procedures. NDBC Tech. Doc. 09-02, 78 pp., https://www.ndbc.noaa.gov/NDBCHandbookofAutomatedDataQualityControl2009.pdf.

O'Reilly, W. C., T. H. C. Herbers, R. J. Seymour, and R. T. Guza, 1996: A comparison of directional buoy and fixed platform measurements of Pacific swell. *J. Atmos. Oceanic Technol.*, **13**, 231–238, https://doi.org/10.1175/1520-0426(1996)013<0231:ACODBA>2.0.CO;2.

Pearson, J., B. Fox-Kemper, R. Barkan, J. Choi, A. Bracco, and J. C. McWilliams, 2019: Impacts of convergence on structure functions from surface drifters in the Gulf of Mexico. *J. Phys. Oceanogr.*, **49**, 675–690, https://doi.org/10.1175/JPO-D-18-0029.1.

——, and Coauthors, 2020: Biases in structure functions from observations of submesoscale flows. *J. Geophys. Res. Oceans*, **125**, e2019JC015769, https://doi.org/10.1029/2019JC015769.

Portilla, J., F. J. Ocampo-Torres, and J. Monbaliu, 2009: Spectral partitioning and identification of wind sea and swell. *J. Atmos. Oceanic Technol.*, **26**, 107–122, https://doi.org/10.1175/2008JTECHO609.1.

Rampersadh, G., 2018: Sea-state interaction based dynamic model of the liquid robotics' Wave Glider: Modelling and control of a hybrid multi-body vessel. M.S. thesis, Dept. of Electrical Engineering, University of Cape Town, 116 pp.

Rogowski, P., M. Otero, J. Hazard, T. Muschamp, S. Katz, and E. Terrill, 2021: XMET—An unattended meteorological sensing system for austere environments. *J. Atmos. Oceanic Technol.*, **38**, 17–30, https://doi.org/10.1175/JTECH-D-20-0016.1.

Schmidt, K. M., S. Swart, C. Reason, and S.-A. Nicholson, 2017: Evaluation of satellite and reanalysis wind products with in situ Wave Glider wind observations in the Southern Ocean. *J. Atmos. Oceanic Technol.*, **34**, 2551–2568, https://doi.org/10.1175/JTECH-D-17-0079.1.

Thomson, J., and J. Girton, 2017: Sustained measurements of Southern Ocean air-sea coupling from a Wave Glider autonomous surface vehicle. *Oceanography*, **30** (2), 104–109, https://doi.org/10.5670/oceanog.2017.228.

——, and Coauthors, 2015: Biofouling effects on the response of a wave measurement buoy in deep water. *J. Atmos. Oceanic Technol.*, **32**, 1281–1286, https://doi.org/10.1175/JTECH-D-15-0029.1.

——, J. B. Girton, R. Jha, and A. Trapani, 2018: Measurements of directional wave spectra and wind stress from a Wave Glider autonomous surface vehicle. *J. Atmos. Oceanic Technol.*, **35**, 347–363, https://doi.org/10.1175/JTECH-D-17-0091.1.

U.S. Weather Bureau, 1963: Manual of barometry (WBAN). 1st ed., U.S. Navy Doc., 1027 pp.

Vaisala, 2012: User's guide: Vaisala weather transmitter WXT520. Vaisala Doc., 171 pp., https://www.vaisala.com/sites/default/files/documents/M210906EN-C.pdf.

Winant, C. D., and A. W. Bratkovich, 1981: Temperature and currents on the Southern California shelf: A description of the variability. *J. Phys. Oceanogr.*, **11**, 71–86, https://doi.org/10.1175/1520-0485(1981)011<0071:TACOTS>2.0.CO;2.

WMO, 2008: Guide to meteorological instruments and methods of observation. 7th ed. WMO Rep. 8, 716 pp.

——, 2018: Guide to instruments and methods of observation. WMO Rep. 8, 548 pp., https://community.wmo.int/activity-areas/imop/wmo-no_8.

Young, R., S. Merrifield, M. Anderson, and E. Terrill, 2021: USV navigation geometry for surface current inference. *OCEANS 2021*, San Diego, CA, IEEE, https://doi.org/10.23919/OCEANS44145.2021.9705780.

Yu, L., 2019: Global air–sea fluxes of heat, fresh water, and momentum: Energy budget closure and unanswered questions. *Annu. Rev. Mar. Sci.*, **11**, 227–248, https://doi.org/10.1146/annurev-marine-010816-060704.

Zhang, Y., C. Rueda, B. Kieft, J. P. Ryan, C. Wahl, T. C. O'Reilly, T. Maughan, and F. P. Chavez, 2019: Autonomous tracking of an oceanic thermal front by a Wave Glider. *J. Field Rob.*, **36**, 940–954, https://doi.org/10.1002/rob.21862.